Supporting Information
to
Imaging Catalytic Hotspots on Single Plasmonic Nanostructures *via* Correlated Super-Resolution and Electron Microscopy

Ningmu Zou, Guanqun Chen, Xianwen Mao, Hao Shen, Eric Choudhary, Xiaochun Zhou, and Peng Chen*
Department of Chemistry and Chemical Biology, Cornell University, Ithaca, New York, 14853

Table of Content

S1. Catalysts preparation and characterization

S1.1. Synthesis of Au nanorods

All commercial materials were used as received unless specified otherwise. All experiments were done at room temperature under ambient aerobic conditions, unless specified otherwise.

Au nanorod synthesis was based on previous work with some modification[1-3]. First, Au nanoparticle seed solution was prepared in a 20 mL aqueous solution containing 2.5×10^{-4} M $HAuCl_4$ (Aldrich) and 2.5×10^{-4} M tri-sodium citrate (Aldrich). After adding 0.6 mL of ice cold 0.1 M $NaBH_4$ solution, the solution turned into wine-red color, indicating the formation of Au nanoparticles of 3-5 nm in diameter. Within 1 h from their formation, these nanoparticles were used as seeds for further growth. Then, Au nanorods were made through a three-step growth procedure: we first prepared a solution with 2.5×10^{-4} M $HAuCl_4$, 0.1 M cetyl-trimethylammonium bromide (CTAB) (Aldrich) and 5.6×10^{-4} M ascorbic acid (Aldrich) in water, and separated the solution into three growth solutions of 9, 18, and 180 mL (labeled as Solution A, B and C, respectively). Then we added 1.0 mL of the seed solution into Solution A. After 20 seconds, 2 mL Solution A was transferred into Solution B. After another 30 seconds, all of Solution B was added into Solution C, which was then shaken and mixed for 10 seconds. Then, Solution C was kept still at 30 °C for 12 hours. The final Solution C contained both gold nanorods, pseudospherical nanoparticles and nanoplates. Solution C was further centrifuged at 600 g-force for 10 minutes. After removing most of the supernatant, the residual solution contained most nanorods. Figure S1 shows the TEM images of as-synthesized Au nanorods.

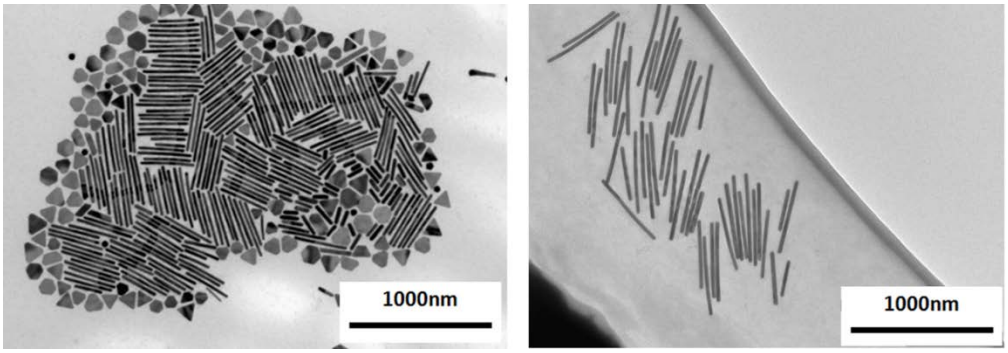

Figure S1. TEM images of as-synthesized gold nanorods.

S1.2. Synthesis of linked Au-Au nanorod-nanorod and Au-Ag nanorod-nanoparticle nanostructures

The linked Au-Au nanorod-nanorod and Au-Ag nanorod-nanoparticle nanostructures were prepared using biotin-streptavidin linkage, following Murphy et al[4] (Figure S2K). First, the nanorod sample from Section S1.1 was diluted by water to 25 mL, which was then mixed with 0.5 mL of 1×10^{-4} M aqueous solution of EZ-Link™ Biotin-HPDP (Thermo Scientific, Catalog No. 21341). After two rounds of stirring, sonication, centrifugation (1000 g-force for 10~15 minutes),removing the supernatant and dilution, most unbound Biotin-HPDP and spherical gold nanoparticles were removed. Pure water was added, diluting the precipitate until the volume was 25 mL. Then, this solution was equally separated to two 12.5 mL batches. After 8 to 12 hours, 0.5 mL 2×10^{-4} M streptavidin (Sigma-Aldrich, Catalog No. S4762) aqueous solution was added into one batch of the solution. After 10 minutes, this solution was centrifuged (1000 g-force for 5 minutes) and most unbound streptavidin could be removed by discarding the supernatant. Then, pure water was added into the streptavidin-coated gold nanorod precipitate until the volume was 2 mL. This streptavidin coated Au nanorod solution was then added dropwise into the other batch of 12.5 mL Biotin-HPDP coated Au nanorod solution. Finally, unlinked gold nanorods could be preferentially removed by

centrifugation (1000 g-force for 10 minutes). Figure S2A-B shows some TEM images of linked Au-Au nanorods.

To prepare the linked Au-Ag nanorod-nanoparticle nanostructure, we used PELCO® NanoXact™ (Ted Pella, Catalog No. 82150-50) 50 nm Ag nanoparticle as the Ag particle precursor. 1 mL Ag nanoparticle solution was diluted by water to a total volume of 12.5 mL and mixed with 0.5 mL of 1×10^{-4} M aqueous solution of EZ-Link™ Biotin-HPDP. After one round of stirring, sonication, centrifugation (1000 g-force for 10 minutes) and removing the supernatant, most unbound Biotin-HPDP was removed. Then, 12.5 mL of previously made streptavidin coated Au nanorod solution was added dropwise into this Biotin-HPDP coated Ag nanoparticle solution. Finally, another centrifugation (1000 g-force for 10 minutes) was applied to remove the unlinked nanorods and nanoparticles in the supernatant. Figure S2C-D shows some TEM images of linked Au-Ag nanorod-nanoparticle structures.

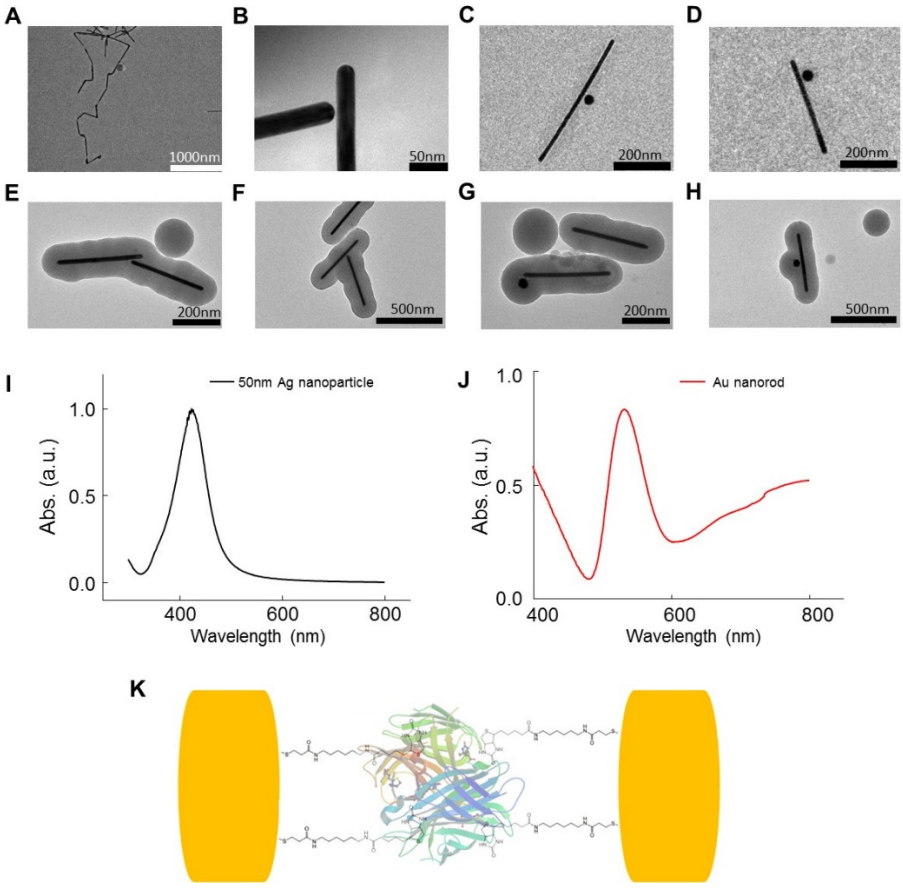

Figure S2. (**A-D**) TEM images of linked Au-Au nanorod-nanorod structures (A-B) and linked Au-Ag nanorod-nanoparticle structures (C-D). (**E-H**) TEM images of linked Au-Au (E, F) and Au-Ag nanostructures (G, H) in mesoporous silica shell. (**I**) Absorption spectrum of 50 nm Ag nanoparticles in aqueous solution, peaking at ~415 nm. (**J**) Absorption spectrum of Au nanorods in aqueous solution with a peak at ~515 nm due to the transverse localized surface plasmon resonance mode. (**K**) Scheme of biotin-streptavidin linked metal nanoparticles.

S1.3. Encapsulation of linked nanostructures with mesoporous silica and subsequent UV-ozone treatment

Both linked plasmonic nanostructures were coated with mesoporous silica shell through the established Ströber method[5], as we previously described in coating individual nanoparticles[3, 6]. In a typical experiment, linked nanostructures were first coated with a thin layer of amorphous silica. Previous linked Au-Au or Au-Ag nanostructure precipitate was diluted into 25 mL aqueous solution. 5 µL of freshly

prepared 20 mM 3-mercaptopropyltrimethoxysilane (MPTMS) in acetone was added while stirring vigorously. After 20 minutes, 1 mL of freshly prepared aqueous solution of 0.54% w/v Na_2SiO_3 (pH 10-11) was added drop wise and left at room temperature for 24 hours under stirring. Then, the reaction solution was centrifuged at 800 g-force for 15 min to precipitate the linked nanostructures, with a thin layer of silica of 2-4 nm in thickness. In order to grow a thicker silica shell, the precipitate was suspended in 25 mL ethanol/water (20 mL:5 mL) solution. Then, 25 µL of tetraethylorthosilicate (TEOS) and 300 µL of 0.1 M NaOH solution were added into the solution. After 24 hours continuously stirring at room temperature, a homogenous silica shell with 80-90 nm thickness could grow on the surface of metal nanostructures. Then, the silica-coated nanostructures were further centrifuged and washed at 1000 g-force for 10 min, to remove the extra NaOH and TEOS.

In order to make silica shell mesoporous, an etching process was used. First, the silica-coated nanostructures were re-suspended in 11 mL ethanol/water (10 mL:1 mL) solution. 70 µL 0.1 M NaOH and 140 µL 0.1 M CTAB were added and the solution was stirred at room temperature for 15 minutes. The solution was put in an oil bath, unstirred, at 90 °C for 2 hours. The mesoporous silica coated metal nanostructures were recovered as precipitates after centrifugation at 1000 g-force for 10 min and were then washed thoroughly, first with ethanol, then with deionized water.

After mesoporous silica shell coating, we used UV-ozone treatment to remove the residue CTAB and other organic species on the nanostructures to activate them for catalysts, as done previously[6, 7]. First, washed nanostructures were dispersed on a glass slide and dried. Then, the sample was placed 10 cm below a 22 W Hg-UV lamp (357 nm, Atlantic Ultraviolet, Catalog No. GPH357T5VH) for 12 hours. The Au nanorods stayed stable under this treatment, as we showed previously[3, 6, 8], but for Ag nanoparticles, some Ag_2O was formed during this treatment, which was subsequently reduced by ascorbic acid[9]. Here the mesoporous silica coated Au-Ag nanorod-nanoparticle structures were treated by 0.5 M fresh ascorbic acid aqueous solution for 8 hours. Then, the solution was centrifuged at 1000 g-force for 5 min to remove the supernatant containing the excess ascorbic acid. The nanostructures after this treatment could be stored in water for weeks.

S1.4. SEM imaging and nanostructure gap size measurement

SEM was done on a LEO 1550VP FESEM operated at 10~15 keV at Cornell Center for Materials Research (CCMR). In order to differentiate the metal cores and mesoporous silica shell, both in-lens secondary electron detector and side-angle detector were used. To be able to see the gap between the two metal nanoparticles within a linked nanostructure, we reduced the noise of SEM images using line averaging. A typical imaging time is about 2 minutes.

To confirm that our SEM imaging condition can indeed reliably determine nanoparticle size, we used TEM as a calibration, by measuring the same batch of as-synthesized Au nanorods. The much higher resolution of TEM allowed us to directly measure the diameter of each Au nanorod through line profiling analysis (Figure S3A, B). In SEM, diameters of Au nanorods were measured by the full width at half maximum (FWHM) of Gaussian fitting the line profiles (Figure S3D, E). Both results from SEM and TEM showed similar mean values and standard deviations (Figure S3C vs. F), indicating the accuracy of diameter measurement in SEM.

Then, we plotted line profiles of gap regions from SEM images by the same method. After subtracting a linear background (Figure S3G, H, upper), we fitted the line profiles of the two particles using Gaussian functions. The Gap size is defined as $d - r_1 - r_2$, where r is the radius of the nanorod/nanoparticle, determined from the FWHM of the Gaussian fit of the line profile, and d is the center-to-center distance between the nanorods/nanoparticles (Figure S3G, H, lower). The measured gap size distribution agrees with the expected dimension of the biotin-streptavidin linkages.[10]

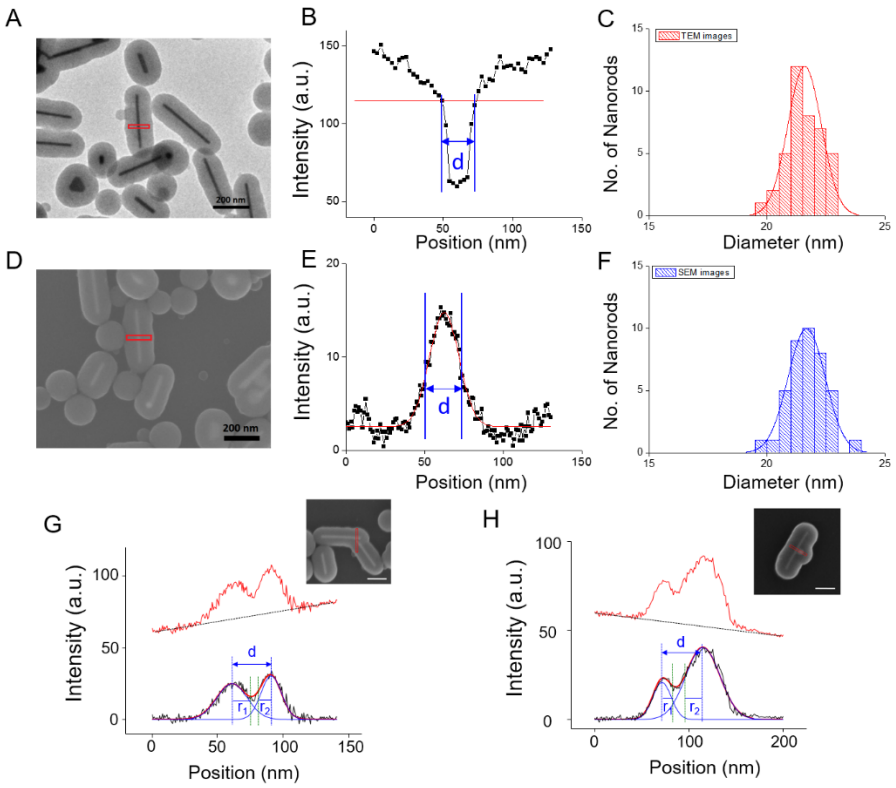

Figure S3. The measured diameter distribution of the same batch of as-synthesized Au nanorods. (**A**) TEM image of mesoporous silica coated Au nanorods. (**B**) Line profile and diameter measurement of the Au nanorod in the red box in A. (**C**) Distribution of Au nanorod diameters from analyzing TEM images; mean diameter is 22.3 ± 0.9 nm. (**D**) SEM image of mesoporous silica coated Au nanorods. (**E**) Line profile and diameter measurement of the Au nanorod in the red box in D. (**F**) Distribution of Au nanorod diameter from analyzing SEM images; mean diameter is 21.6 ± 0.8 nm. (**G**) The linear background subtraction from the SEM line profile for a linked Au-Au nanorods; same as main text Figure 1A. (**H**) Same as G, but for a linked Au-Ag nanorod-nanoparticle; same as main text Figure 1F. Inset in H and G are corresponding SEM images of linked nanocatalysts with line profile analysis red box. All scale bars are 200 nm.

S1.5. EDX elemental analysis

To further confirm the identity of linked Au-Ag nanorod-nanoparticle structures, we used EDX elemental analysis. The EDX was done using a Bruker Quantax x-ray Detector attached to the SEM. Besides those peaks from carbon, oxygen, sodium, silicon, which were introduced from the carbon coating, and mesoporous silica shell and buffer solution residue, we can clearly see the presence of both Au (M line at 2.12 keV) and Ag (Lα line at 2.98 keV) (Figure S4). The EDX elemental analysis results also agree with the optical microscopy analysis of scattering vs. emission intensities (Figure 3 in the main text), further proving the composition of linked nanostructures.

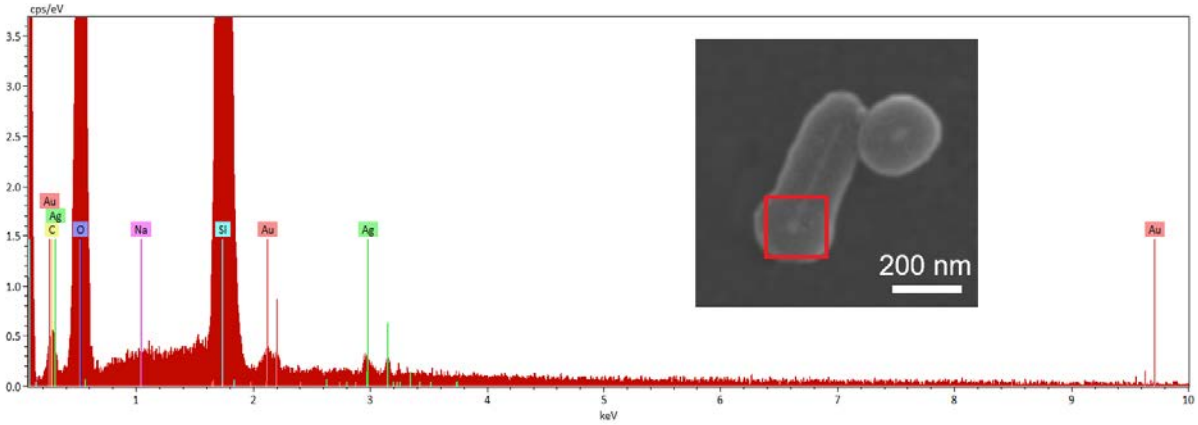

Figure S4. An EDX spectrum of a linked Au-Ag nanorod-nanoparticle structure. The red box of the inset shows the area where the EDX spectrum was measured.

S1.6. Biotin-streptavidin linkage increases the yield of linked nanostructures by ~7 times

We compared the yield of linked Au-Au nanorods with and without using the biotin-streptavidin linkage. Without the biotin-streptavidin linkage, the linked nanorods could also form by chance. Figure S5 shows the SEM images of mesoporous silica coated Au nanorods with and without biotin-streptavidin linkage procedure. The linkage efficiency increases by about 7 times with the biotin-streptavidin linkage method.

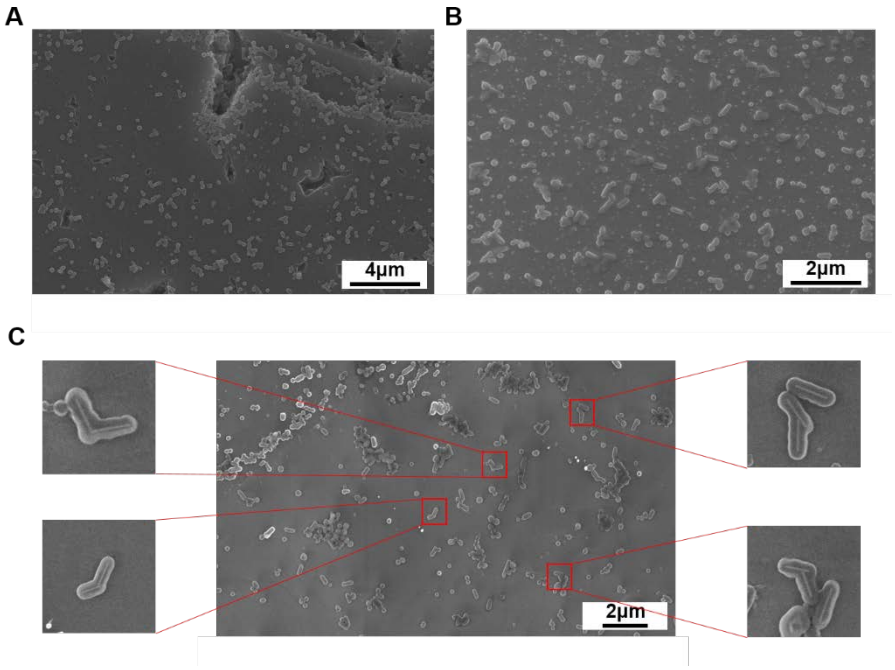

Figure S5. (**A-B**) SEM images of mesoporous silica coated Au nanorods without using biotin-streptavidin linkage procedure. The linkage efficiency is ~4% (3 linked nanorods out of 82 nanorods). (**C**) SEM images of mesoporous silica coated linked Au-Au nanorods after biotin-streptavidin linkage procedure. The linkage efficiency is ~27% (21 linked nanorods out of 79 nanorods), 7 time larger than in A and B.

S1.7. Ascorbic acid treatment can reduce surface Ag_2O formed during UV-ozone treatment

To probe if ascorbic acid can indeed reduce the Ag_2O layer formed during UV-ozone treatment, we used pure Ag nanoparticles and measured their emission signal brightness excited by 405 nm laser before and after UV-zone treatment.

Ag nanoparticle emission intensity was examined under an optical microscope with 20 mW 405nm laser excitation. To detect the emission signal, a 425 nm long-pass filter was applied. The emission signal was measured for 100 Ag nanoparticles before/after UV-ozone treatment and ascorbic acid reduction. The result shows that the emission signal intensity decreases after UV-ozone treatment, due to the partial oxidation of surface Ag atoms (Figure S6A-B). After ascorbic acid treatment, the emission signal intensity increases back, indicating the reduction of silver oxide (Figure S6C). For the linked Au-Ag nanostructures, Ag surface was protected by residual CTAB before UV-ozone treatment, which would be first oxidized by ozone. Therefore, the smaller amount of oxidized Ag atoms on the surface could be reduced more easily that bare Ag nanoparticles, and its effect on surface plasmon would be even less significant.

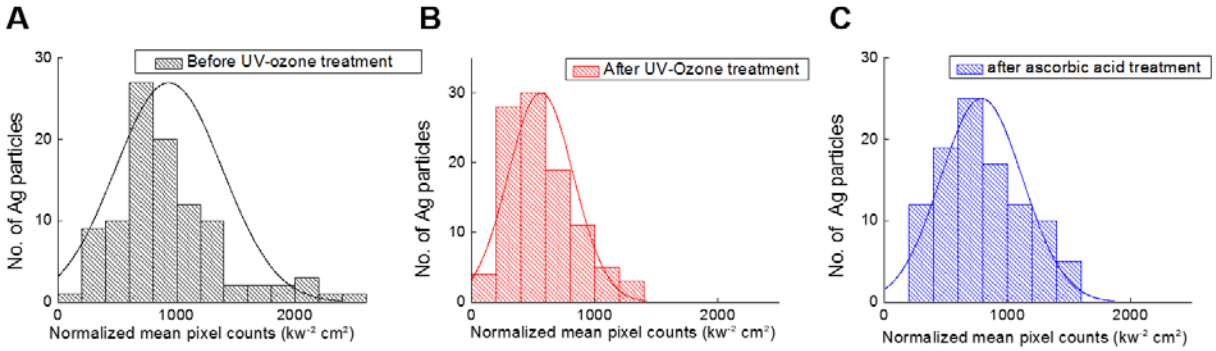

Figure S6 (**A**) Histogram of pixel counts of emission signals from 100 Ag nanoparticles before UV-ozone treatment; the average intensity is 933.8 ± 449.1. (**B**) Histogram of pixel counts of emission signals from 100 Ag nanoparticles after UV-ozone treatment; the average intensity is 560.2 ± 264.9. (**C**) Histogram of pixel counts of emission signals from 100 Ag nanoparticles after ascorbic acid treatment; the average intensity is 788.7 ± 332.8. The pixel counts were taken from a 3×3 pixel window for averaging and normalized by the local incident 405 nm light intensity. Lines are Gaussian fits.

S2. Single-molecule fluorescence microscopy of catalysis

S2.1. Single-molecule fluorescence imaging of catalysis on plasmonic nanostructures

All single-molecule fluorescence experiments were done on a homebuilt prism-type total internal reflection fluorescence (TIRF) microscope based on an Olympus IX71 microscope (Figure S7A, B)[3, 6]. For both linked Au-Au nanorod-nanorod and Au-Ag nanorod-nanoparticle catalysts, a continuous wave circularly polarized 532 nm laser beam (CrystaLaser GCL-025-L-0.5%) of 23 mW was directed onto the sample to excite the fluorescence of the catalytic product resorufin. For linked Au-Au nanorod-nanorod catalyst, because its transverse mode of LSPR is around 520 nm,[11] no other laser was needed to excite its LSPR. For linked Au-Ag nanorod-nanoparticle catalyst, the LSPR of 50 nm Ag nanoparticle is around 400 nm[12, 13], and a second CW circularly polarized 405 nm laser beam (CrystaLaser DL405-100-O) was used to excite the Ag LSPR preferentially with a power range of 0~50 mW. The fluorescence of the product resorufin was collected by a 60× NA1.2 water-immersion objective (UPLSAPO60XW, Olympus), filtered (HQ580m60, Chroma), and detected by a back illuminated ANDOR iXon EMCCD camera (DU897D-CS0-#BV) operated at 30 milliseconds frame rate.

We used reductive deoxygenation of resazurin to resorufin by NH_2OH as a probe reaction to test the catalyst activities (Figure S7C). We have previously shown[14] that Au nanoparticles are active in catalyzing this reaction. Ag, on the other hand, are inactive, shown by the ensemble activity measurements

(Figure S7E). In single molecule fluorescence experiments, the aqueous reactant solution containing 200 nM resazurin, 6 mM NH_2OH in pH 7.2 100 mM phosphate buffer was continuously fed into a microfluidic reactor cell (~ 0.1 mm in height × 5 mm in width × 50 mm in length) with a syringe pump (Chemyx Fusion 200) at 20 μL/min. The concentration of resazurin was chosen as 200 nM at which the catalytic kinetics was approaching saturation and less sensitive to its concentration (Figure 7B-C in the main text)[14].

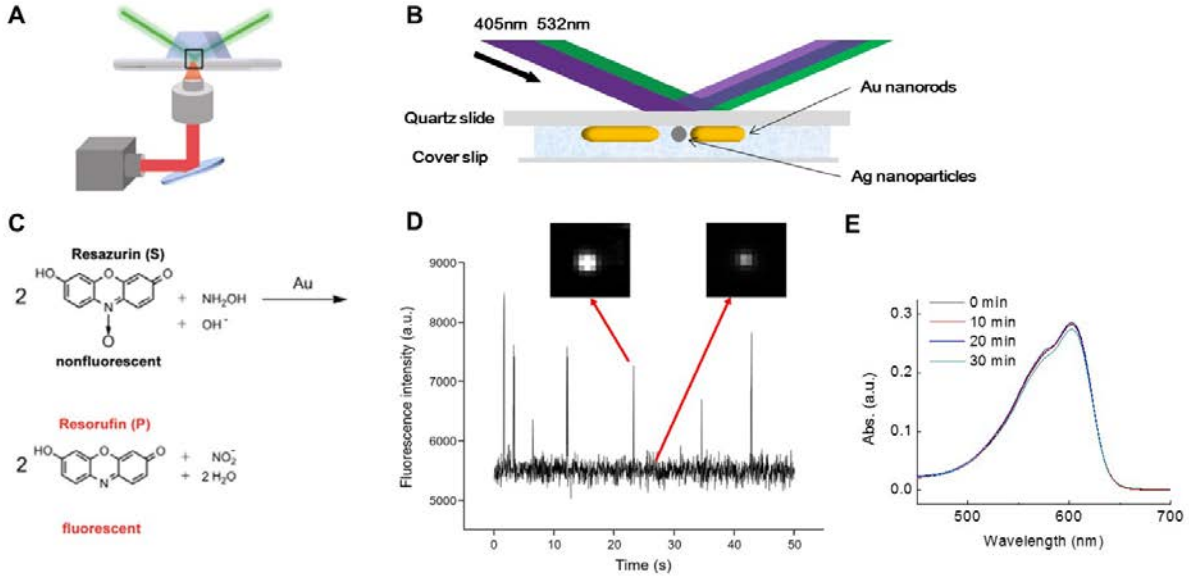

Figure S7. Single molecule fluorescence imaging of catalysis on plasmonic metal nanostructures. (**A, B**) Simplified scheme of the flow cell and camera set-up. The total internal reflection laser excitation illuminates an area of $\geqslant 100 \times 50$ μm^2. Figure A adopted from our earlier publication.[8] (**C**) Reaction schemes: the fluorogenic reductive deoxygenation of the nonfluorescent resazurin molecule (denoted as S) to the fluorescent resorufin (denoted as P) by NH_2OH, catalyzed by Au nanorods. (**D**) Exemplary fluorescence intensity trajectory of the Au-Au nanostructure in Figure 2A in the main text under catalysis. Insets are single frame images of the nanostructure with (left) or without (right) a fluorescent catalytic product molecule. (**E**) Absorption spectra of a solution containing 5 μM resazurin and 1 mM NH_2OH in the presence of 0.25 mL Ag nanoparticles (2.90 x 10^{10} particle/mL). No formation of the product resorufin (λ_{abs} ~570 nm) was observable, indicating Ag nanoparticles are catalytically inactive here.

S2.2. Data analysis of single-molecule super-resolution fluorescence imaging of catalytic events on individual plasmonic nanostructures

Individual catalytic product formation events on each linked Au-Au and Au-Ag nanostructures were detected by the product fluorescence image and localized in position to nanometer precision. The general data processing methods followed our previous reports using home-written MATLAB codes[3, 6, 8].

First, we identified the individual nanocatalysts in both SEM and scattering/fluorescence images. Both Au and Ag nanostructures scatter laser light strongly and are emissive, and are thus readily identifiable in the optical microscope. We then extracted the fluorescence intensity trajectory of each nanostructure under catalysis from the recorded fluorescence movies by integrating the EMCCD counts over a 7×7 pixels area (each pixel ~267 nm) around the nanostructure. The bursts of fluorescence intensity on top of the background emission signal of the nanostructure were due to catalytic formations of the product resorufin molecules. Then, we used intensity thresholds to select the fluorescence burst events. After cropping out an area of 13 × 13 pixels (~3.5 ×3.5 μm^2) around the product molecule, all image frames contributing to the same single burst were added together to enhance the signal to noise ratio. From this image, the background emission signal of the nanostructure was subtracted, as we detailed previously[3, 6]. Briefly, we first extracted the fluorescence intensity trajectory of each single nanostructure under catalysis from the recorded

fluorescence movie. The fluorescence intensity of a single Au-Au or Au-Ag nanostructure in each fluorescence image was obtained by integrating the EMCCD counts over a 7×7 pixel area, which is sufficiently large to ensure encompassing the nanostructure and any fluorescent catalytic product molecules entirely. Figure S7D shows an exemplary fluorescence intensity trajectory of the linked Au-Au nanorod in Figure 2A in the main text. The trajectory shows bursts of fluorescence intensity on top of the background emission signal of the nanorod itself.

We then selected fluorescence bursts from the trajectory of a nanostructure under catalysis, according to a threshold determined by Gaussian fitting the histogram of fluorescence intensity trajectory. Next, we identified the corresponding image frames of each burst in the fluorescence movie for subsequent analysis to determine the locations of catalytic reactions. Here, each burst is a result of catalytic generation of a resorufin product molecule from a single nanostructure. To determine the center position of the fluorescence PSF of a single product molecule in its fluorescence image, an image area of 13 × 13 pixels around the molecule was cropped out for 2-D Gaussian fitting. For each detection of a product molecule, all image frames (e.g., Figure S7D left inset) contributing to the fluorescence burst were combined to form a single image. Because both Au-Au and Au-Ag nanostructures are emissive under the excitation of 532 nm or 405 nm laser, the emission signal of the nanostructure itself (e.g., Figure S7D right inset) was subtracted; here the nanorod emission signal was taken from the image frames right before the appearance of the burst signal in the movie. The resulting image only contained the fluorescence signal of the catalytic product molecule resorufin. Then the image of the molecule, which behaves as a point spread function (PSF), was fitted by a two-dimensional Gaussian function (Equation (S1)) to obtain the center position (x_0, y_0) of the PSF, which reflects the position of the product molecule.

$$A\,(x,y) = \int_{x-\delta}^{x+\delta} dx \int_{y-\delta}^{y+\delta} dy\, A_0 \exp\left[-\frac{1}{2}\left(\frac{x-x_0}{\sigma_x}\right)^2 - \frac{1}{2}\left(\frac{y-y_0}{\sigma_y}\right)^2\right] + Bx + Cy + D \qquad \text{(S1)}$$

In Equation (S1), $A(x, y)$ is the intensity of a single molecule signal at position (x, y) in the corresponding image. $Bx+Cy+D$ accounts for the image background. δ is half of the pixel size. σ is the standard deviation of the two-dimensional Gaussian function along x or y direction and reflects the width of the PSF.

Due to a large number of fluorescence photons detected, the center position of each product molecule can be localized down to a few nm accuracy[15, 16], but often around 35-45 nm in this study due to the short residence time of the product on the catalyst. To reduce the contribution of noises to the selected burst events, we further filtered the selected burst events by their localization accuracies and the widths of the fitted PSF (i.e., σ_x and σ_y in Equation (S1)), as we described previously[8].

During the experiment, every movie would last for at least one hour. The flow cell could drift with sample stage. The center positions of all molecules were further corrected for microscope stage drifting, by using the intrinsic emission signal of Au nanoparticles as position markers. Similarly as described above, PSF of nanoparticle emission was fitted with a 2D Gaussian function while its center position was tracked throughout the course of the experiment. The fluorescence bursts due to product formations were excluded from this analysis. In each movie, average drifting of at least five position markers was used to correct for sample stage drift.

The positions of catalytic product molecules on a single nanostructure can be overlaid together in a scatter plot and correlated with the SEM image of the nanostructure, whose structural contour was determined from the SEM image. Their correlation with SEM image could be directly mapped using position markers, which is described below (Section S4). Once the structural contour of a nanostructure was mapped on top of the positions of catalytic products, the nanostructure could be dissected into gap regions and non-gap regions. Finally, product molecules were sorted to their corresponding regions, based on their positions.

S2.3. Correcting for detection efficiency differences at different laser power densities

In our single-molecule fluorescence imaging experiments, the detection efficiency of the fluorescent product molecules could depend on the local power density of the 532 nm laser that was used to induce the product fluorescence (as well as excite the Au surface plasmon). To address potential unequal detection, we need to correct the number of product detection events according to their local power density of the 532 nm laser. We thus performed a simulation to determine the correction for the efficiency of single-molecule detection. Figure S8 shows the general method of this process.

First, we obtained the distribution of σ_x, σ_y, A_0 in 2-D PSF Gaussian fitting (Equation (S1)) of the experimental single-molecule fluorescence images (Section S2.2). For example, Figure S8A-B show the σ_x and σ_y distributions of >7000 events detected on a single linked Au-Au nanorod nanostructure under 532 nm laser excitation with incident power density at 1.80 kW cm^{-2}. We could then determine the mean values and standard deviations from the distributions of σ_x and σ_y, by approximating that they follow a normal distribution (red curves in Figure S8A-B). Similarly, for the same nanostructure, we could obtain the distribution of A_0 and approximate that it follows a Gamma distribution (red curve in Figure S8D). Then, the background level of the experimental image under the same incident power density was obtained from any of the pixels that are three pixels away from the same nanostructure. The distribution of background pixel counts follows a normal distribution (Figure S8C).

After obtaining the information above, we could simulate single-molecule fluorescence images under the same incident power density. First, we constructed 1000 background image frames. All pixel counts in these frames are randomly sampled from the distribution in Figure S8C. Second, in order to simulate a single-molecule fluorescence detection event centered at a position (x_0, y_0), we randomly sampled the values of σ_x, σ_y, and A_0 from the parameterized distributions we obtained in Figure S8A-B and Figure S8D. Third, by using the 2-D Gaussian equation (S2), we could construct a simulated single-molecule fluorescence image centered at any position in any image frame, by adding the $A(x, y)$ value to pixels in the background frames. To simplify the simulation, the range of each simulated PSF is 7×7 pixels. Each pixel is 266 nm × 266 nm, which is the real pixel size in our experimental single-molecule fluorescence movies.

$$A\,(x,y) = A_0 \exp\left[-\frac{1}{2}\left(\frac{x-x_0}{\sigma_x}\right)^2 - \frac{1}{2}\left(\frac{y-y_0}{\sigma_y}\right)^2\right] \quad \text{(S2)}$$

Then, we simulated a 6×6 nanostructure matrix with 100 catalytic fluorescent product events on each of them (Figure S8E). These 100 catalytic products were temporally distributed evenly over the 1000 movie frames (1 on-time frame with next 9 off-time frames). Finally, we had a simulated 1000-frame movie, and this movie represented the scenario under a certain local incident power density. To simulate conditions under different incident laser power densities, we chose another experimentally measured nanostructure with a different local laser power density and repeated the protocol above. Here, we performed the simulations under 4 different incident local power densities to cover our experimental range (Figure S8F).

Ideally, if our single-molecule fluorescence image analysis detection algorithm is selective enough, all 100 catalytic events would be detected so that detection efficiency would be 100%. However, some events would miss detection during image analysis due to limited single-to-noise ratios. This loss is observed when we performed the same image analysis procedures on the simulated fluorescence movies, where high local laser power density is expectedly accompanied with higher detection efficiency (Figure S8F). In order to correct for this to be unbiased in the determination of the actual turnover rates, we normalized the detection efficiency by setting the value at the highest 532 nm laser power density as 1 and we got:

$$\eta = 0.0529\, I + 0.9048 \qquad \text{(S3)}$$

in which η represents the detection efficiency and I represents the 532 nm laser power density in unit of kW cm^{-2}. Then, Equation (S3) was applied to all single-molecule experimental data to correct detection efficiency. Please note that even at the lowest incident power density, the detection efficiency is only ~6% less than that at the highest power density; so, this correction does not significantly change the trend of catalytic turnover rates vs. incident laser power densities.

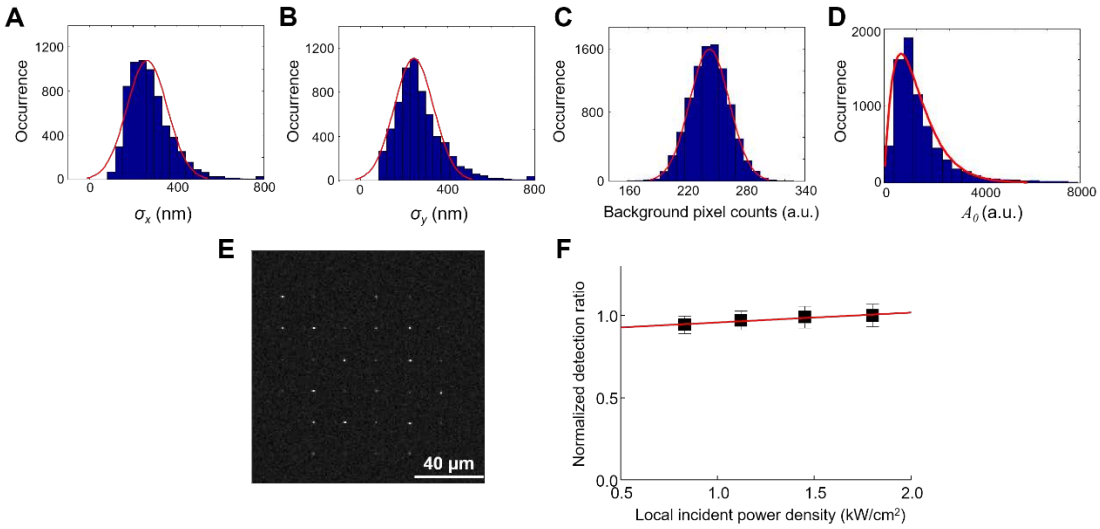

Figure S8. Signal detection efficiency correction for differences in local laser power densities. (**A, B**) σ_x and σ_y distributions of single-molecule fluorescence detection events from a linked Au-Au nanorod under 532 nm laser excitation with incident power density of 1.80 kW cm^{-2}. (**C**) Distribution of the pixel count at a pixel three pixels away from the same nanostructure in A-B. Data were collected from more than 10000 experimental movie frames. The incident power density at this pixel is considered the same as the nanostructure besides it. Red curves in A-C are fits with a normal distribution. (**D**) Distribution of intensity A_0 in Eq (S1) from the same nanostructure in A-B. Red curve is a Gamma distribution fit. (**E**) One frame of the simulated fluorescence image in a movie on 36 nanostructures under 532 nm laser excitation with incident power density at 1.80 kW cm^{-2}, arranged in a 6×6 matrix with 20 μm distance between one another. (**H**) Fluorescence signal detection efficiencies under different 532 nm laser power densities, in which the efficiency at the highest laser power density (1.80 kW cm^{-2}) is set as one. Red line is a linear fit. Error bars represents s.d.

S2.4. Calculating the local incident laser power from evanescent field excitation via TIR

In the single-molecule imaging experiment, the 532 nm, 405 nm, or both lasers were used to illuminate the nanocatalysts through TIR mode. In calculating the local incident power density, we also considered the evanescent field generated at the quartz-water interface, where the nanocatalysts reside. TIR excitation makes use of the exponential decay of the evanescent field generated upon total internal reflection at a high-index to low-index boundary (here is the quartz-water boundary). The intensity $I(z)$ of evanescent wave at a distance z away from the interface follows:[17]

$$I(z) = I(0)e^{-\frac{z}{d}} \qquad \text{(S4)}$$

Here $I(0)$ is the intensity at the interface, which depends upon both the incident angle and the polarization of incident beam, and the exponential decay distance is

$$d = \frac{\lambda_0}{4\pi\sqrt{n_2^2 sin^2\theta - n_1^2}} \quad \text{(S5)}$$

where λ_0 is the wavelength of the excitation light in vacuum; n_1 is the refractive index of water; n_2 is the refractive index of quartz, and θ is the incidence angle.

For a light beam with *s*-polarization, $I(0)$ is:

$$I_s(0) = I_s \frac{4\cos^2\theta}{1 - n^2} \quad \text{(S6)}$$

where I_s is the *s*-polarized incident light intensity on the quartz slide, $n = n_1/n_2$.

For a light beam with *p*-polarization, $I(0)$ is:

$$I_p(0) = I_p \frac{4\cos^2\theta(2\sin^2\theta - n^2)}{n^4\cos^2\theta + \sin^2\theta - n^2} \quad \text{(S7)}$$

where I_p is the *p*-polarized incident light intensity on the quartz slide.

In our experiment, the incident light is circularly polarized, which means the light intensities of both the *s*- and *p*-polarized light components, I_s and I_p, are the same as half of the original light intensity I_0.[18] Therefore, $I(0)$ in Equation (S4) should be the summation of $I_s(0)$ and $I_p(0)$ in Equations (S6) and (S7). To calculate the light intensity at the nanocatalyst in the TIRF excitation, *z* in Equation (S4) was approximated as the average thickness of mesoporous silica shell plus half of the nanorod diameter. After applying other experiment parameters (i.e., θ = 67.2°, n_1 = 1.33 and n_2 = 1.46) into equation (S4). We obtained:

$$I_{local}^{532nm} = 2.96\, I_0^{532nm}$$
$$I_{local}^{405nm} = 2.79\, I_0^{405nm} \quad \text{(S8)}$$

We have used Equation (S8) for calculating the local incident laser power and power density.

S3. Linked plasmonic nanostructures do not show discernible deactivation of catalytic activity over the course of our single-molecule experiments

Our catalysis imaging duration for catalytic reactions was about 3~5 hours for each experiment in which we always used freshly synthesized linked nanostructures. To evaluate if there was any significant deactivation of catalytic activity during reaction, we imaged reactions over 5 hours while keeping the reaction conditions unchanged (concentration of resazurin was at 200 nM). No significant changes in turnover rates are discernible over ~5 hours for the linked Au-Au nanorods, for example (Figure S9), and therefore, these linked nanostructures are stable in activity during our experimental observation time. It is worth noting that we did observe significant deactivation a week after the nanocatalysts were synthesized.

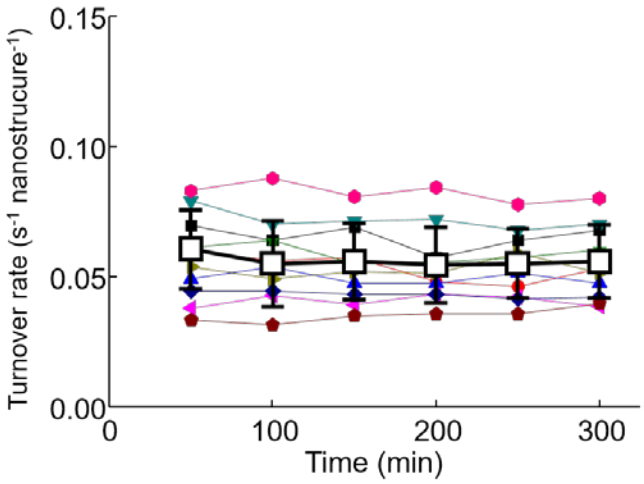

Figure S9. Time profiles of turnover rates of 10 individual linked Au-Au nanorods (solid symbols) and their averaged behavior (hollow squares) over 5 hours. Error bar are s.d.

S4. Image correlation between super-resolution fluorescence microscopy and SEM

To correlate the structure of linked plasmonic nanostructures to the super-resolution mapping of its catalytic products, nanometer precision mapping between the fluorescence images and SEM images is needed. Direct overlaying of these two types of images is not sufficiently precise due to the slight image distortion, especially in SEM which uses line scanning to form an image, during which the sample could move slightly.

We used symmetric isolated single nanocatalysts (e.g., nanoparticle, nanorods) near the linked Au-Au or Au-Ag nanostructures as position markers to improve the accuracy of overlaying SEM and super-resolution fluorescence images. First, SEM image (Figure S10A) contours of individual nanostructures were extracted by using Sobel edge detection algorithm in MATLAB code (Figure S10B). After obtaining a binary gradient mask from edge detection, we determined the center position of each marker using the mass center of contours (red dots in Figure S10B). Meanwhile, in the super-resolution image of catalytic products, the center position of every symmetric nanocatalyst was calculated by averaging all coordinates of catalytic products on top of it (white circles in Figure S10C). After obtaining the two sets of coordinates from the SEM image and the super-resolution catalysis image, we randomly chose a pair of nanoparticles and used them as markers to overlaying the two images together. One nanoparticle of the pair is set as the origin with coordinates (0, 0) in both images. The other nanoparticle and its coordinates were transformed by Equation (S9) including rotation and magnification transformation.

$$\begin{bmatrix} x' \\ y' \end{bmatrix} = \boldsymbol{A} \begin{bmatrix} \cos\theta & -\sin\theta \\ \sin\theta & \cos\theta \end{bmatrix} \begin{bmatrix} x \\ y \end{bmatrix} \quad \text{(S9)}$$

After obtaining values of $\boldsymbol{A}$ and θ, we applied this transformation matrix to all other nanoparticle marker coordinates in the images. Because of the distortion, other nanoparticles may not be perfectly overlaid. Then, we calculated the summation of distance differences of these other nanoparticle markers and used this summed difference as a criterion to evaluate the overlaying procedure. We iteratively tried all combinations of pairs using the same algorithm to find the optimal $\boldsymbol{A}$ and θ, which can minimize the summation of distance differences. Figure S10D shows the distance error distribution from all transformation matrices in the same set of position markers. This optimization process provides overlaying

error of ~7.8 nm on average, which is much smaller than the spatial resolution of our single-molecule super-resolution imaging experiments (~40 nm here).

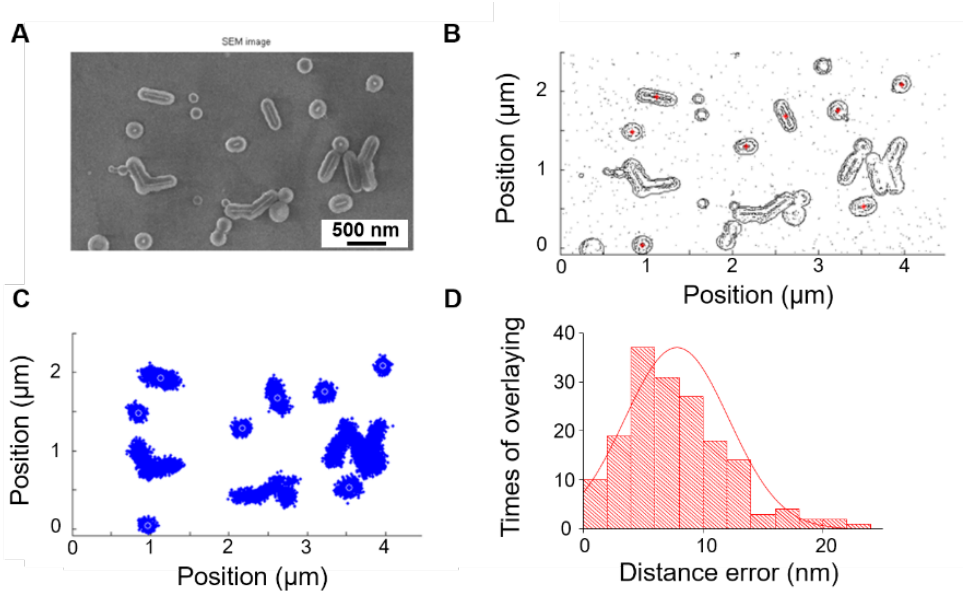

Figure S10. Overlaying SEM and super-resolution image of catalytic products. (**A**) SEM image of the sample. (**B**) Binary gradient mask from edge detection of image in A. Red dots represent mass centers of symmetric nanoparticles. (**C**) Locations of catalytic products from all nanoparticles in A. White circles represent mass centers of products from symmetric nanoparticles. (**D**) Distribution of overlaying distance errors of 6 nanoparticles besides the 2 chosen markers out of the 8 nanoparticles in B; the 2 markers were iterated among all possible pairs out of the 8 total.. The mean error is 7.8 ± 4.2 nm.

S5. Other possible mechanisms of catalytic hotspots at gap regions and the rationales against them

S5.1. Additional results to show that (1) the observation circle size does not change the gap vs. non-gap activity ratio (Figure S11); (2) there is no fluorescence intensity enhancement or increased product molecule residence time at gap regions (Figure S11); (3) there is no enhanced catalytic activity at the region between two adjacent nanorods (>90 nm apart) (Figure S12A-B); and (4) the fluorescence intensity threshold in image analysis does not affect the spatial pattern of the product locations (Figure S12C-E) or the spatial pattern of the product fluorescence intensities (Figure S12F-H).

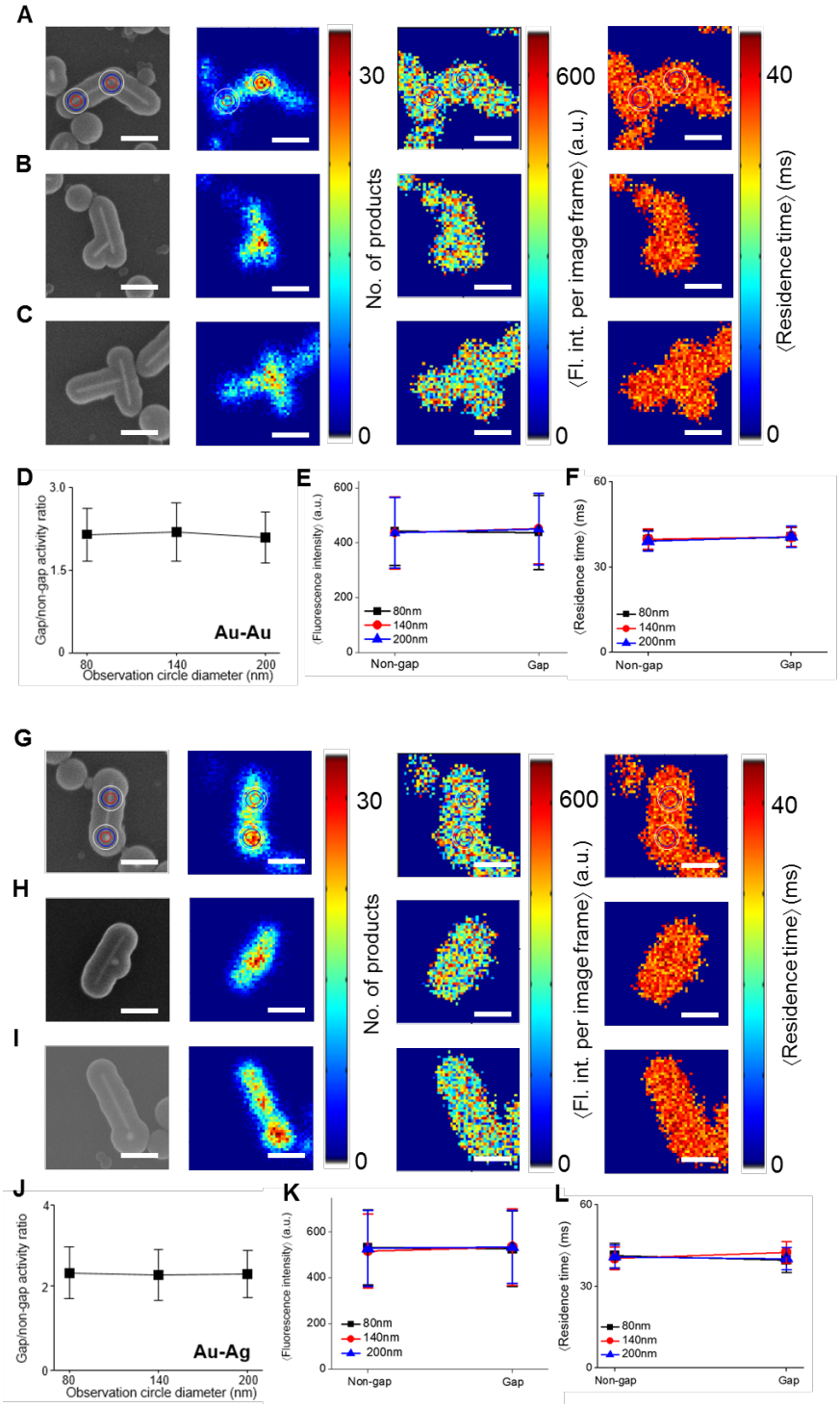

Figure S11. The observation circle size does not change the gap vs. non-gap activity ratio or the average fluorescence intensities of individual product molecules in each image, and their average residence times at gap vs. non-gap regions do not differ significantly for both linked Au-Au and Au-Ag plasmonic nanocatalysts. (**A-C**) Three additional examples of SEM image (1st column), 2-D histogram of the detected reaction products (2nd column), spatial pattern of the average fluorescence intensity per frame (3rd column), and spatial pattern of the average residence time (4th column) of the individual fluorescent product molecules on linked Au-Au nanocatalysts. (**D**) Gap vs. non-gap activity ratio for all 31 linked Au-Au nanorods with different observation circle diameters from 80 nm to 200 nm. (**E**) Average fluorescence intensities of the product molecules at gap and non-gap regions at different observation circle diameters, for 31 linked Au-Au nanorods. (**F**) Average residence time at gap and non-gap regions

with different observation circle diameters, for 31 linked Au-Au nanorods. (**G-I**) Same as A-C, but for three additional examples of linked Au-Ag nanocatalysts. (**J-L**) Same as D-F, but for 29 linked Au-Ag nanostructures. Y-axis error bars represent standard deviation. All scale bars represent 200 nm.

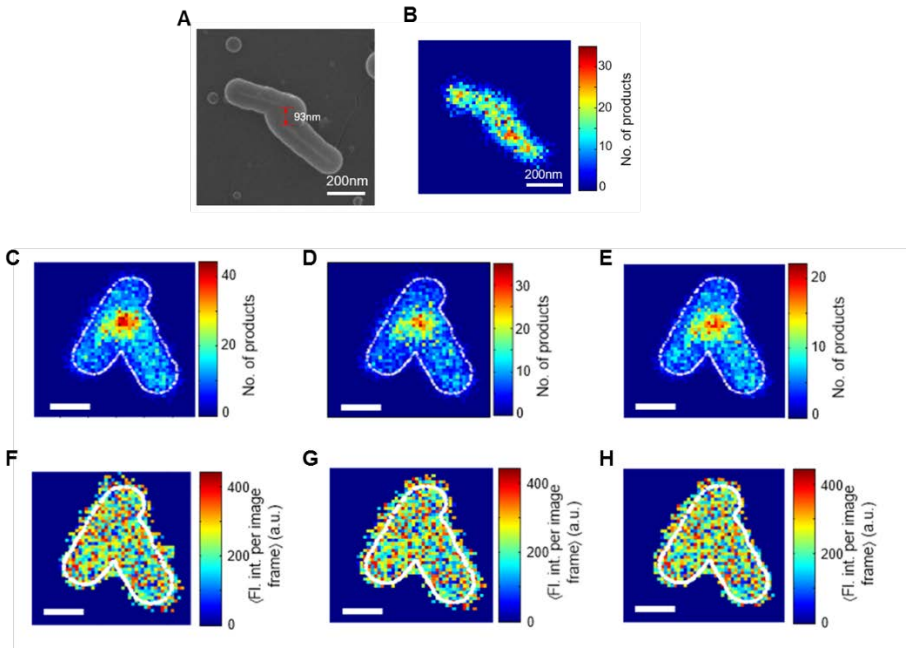

Figure S12. (**A-B**) SEM (A) and product location histogram (B) of two adjacent Au nanorods with fused $mSiO_2$ shell, where the closest distance is 93 nm. No enhanced catalytic activity is observed at the region between the two nanorods **(B)**. (**C-E**) Fluorescence intensity threshold does not affect the spatial distribution patterns of the detected product numbers and their average fluorescence intensities. The fluorescence signal of catalytic products on nanostructure in Figure 2 of the main text were analyzed with different thresholds as 3.0σ (C), 3.5σ (D), and 4.0σ (D) of the whole intensity vs. time trajectory (see Section S2.2). (**F-H**) The corresponding spatial distribution of the average single-molecule fluorescence intensities per image frame of the catalytic product resorufin.

S5.2. Product rebinding experiment shows equal molecular accessibility at the gap and non-gap regions

To ensure that the detected activity differences at the gap and non-gap regions are not due to differences in the local reactant access to the metal surface through the mesopores of the $mSiO_2$ shell, we performed a control experiment in which we flowed 1 nM resorufin into the microfluidic reactor and imaged resorufin binding to the linked Au-Au nanorods encapsulated in mesoporous silica shell (Figure S13A-B). Here, the binding of resorufin, which is structurally similar to resazurin, probes the accessibility. Based on the background fluorescence level in the microfluidic reactor, which is proportional to the concentration of resorufin in the solution, this 1 nM concentration of resorufin is about 10 times larger than the steady-state concentration of resorufin generated during resazurin deoxygenation reactions catalyzed by Au nanocatalysts under similar laser excitation and solution flow conditions.

Using the detected resorufin binding events on single linked Au-Au nanorods in this control experiment, we calculated the event detection rates at both the gap and non-gap regions with different observation circle diameters. The detected event is about 10 times less than that in the catalytic reduction of resazurin, as expected. More important, there is no significant difference in the resorufin binding rate at the gap vs. non-gap regions, and the ratio is about 0.97 ± 0.11 (Figure S13C and D). Therefore, the observed activity differences at the gap and non-gap regions are not due to different reactant accessibility.

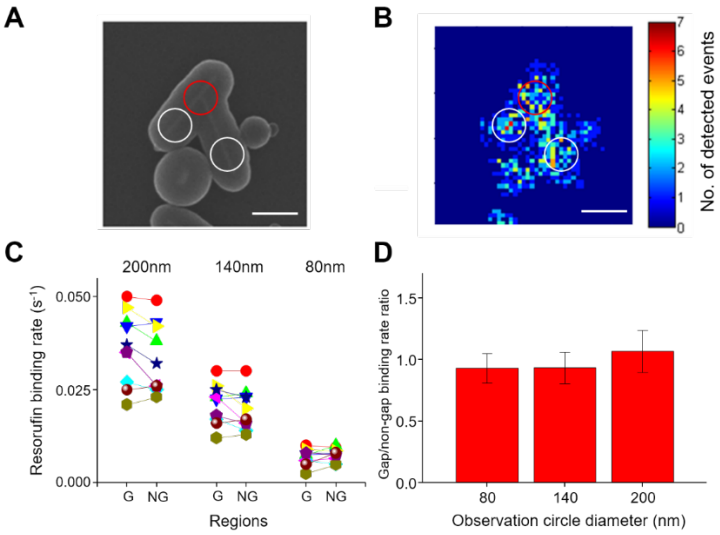

Figure S13. (**A**) SEM image of a linked Au-Au nanorod. Red and white circles represent the gap and non-gap regions (140 nm diameter here). (**B**) 2-D histogram of detected resorufin binding events on the nanostructure in A. All scale bars are 200 nm. (**C**) Resorufin binding rate with different observation circle diameters at gap (G) and non-gap (NG) regions of individual linked nanostructures. Each pair of linked symbols represents a single nanostructure. (**D**) Average resorufin binding rate ratio of gap vs. non-gap regions of individual linked Au-Au nanostructure with different observation circle diameters.

S5.3. Thermal effect should not be the activity enhancement mechanism

Another potential mechanism for the catalytic hotspots at gap regions is the temperature increase caused by the plasmonic thermal effect. However, this mechanism would not generate any spatial temperature heterogeneity within a single nanostructure due to the high thermal conductivity of Au and Ag, which would make the thermal effect homogenous across a single nanostructure.

To probe the spatial and temporal profile of temperature on our nanocatalyst, we used the 1-D thermal diffusion equation to examine the heat dissipation[19]:

$$\frac{\partial T}{\partial t} = \alpha \frac{\partial^2 T}{\partial x^2} = \frac{k}{\rho c_p} \cdot \frac{\partial^2 T}{\partial x^2} \quad \text{(S10)}$$

in which α is the thermal diffusivity of the material, k is its thermal conductivity, ρ is its density, and c_p is its specific heat.

In our experiments, the incident light power density is between 0.6 ~ 2 $\times 10^3$ W/cm^2. The diameter of nanorods we used is about 20 nm. As the heat generation is only due to the excitation of the transverse SP mode of Au nanorod (~510-540 nm) by the 532 nm laser and a previous research[20] demonstrated that the Au nanoparticles with similar size only show a maximal temperature increase of 1 K, we chose a 5 K initial temperature increase at the center, which would be an overestimate of the upper bound of the temperature increase. Moreover, we assume the dimension of material is 400 nm in length. Since all experiments were conducted in a microfluidic flow cell with continuous solution flow at room temperature, the boundary condition for solving the differential equation (S10) is that $\frac{\partial T}{\partial t} = 0$ at x = 200 or -200 nm, i.e., there is no temperature change at the edge of material due to the thermal bath provided by the surrounding solution environment. We simulated temperature profiles using different materials, including water, silica, gold and silver. Other parameters in this simulation are shown in Table S1.

Table S1. Parameters for heat dissipation simulations. All values are from CRC Handbook of Chemistry and Physics.

Material	Thermal Conductivity k (W • m^{-1} • K^{-1})	Density ρ (kg • m^{-3})	Specific Heat c_p (J • kg^{-1} • K^{-1})
Water	0.58	1000	4180
Silica	1.30	2648	703
Gold	310	19320	129
Silver	429	10490	233

Figure S14A and B show the simulated time-dependent temperature profile along one dimension for water and gold. For water and silica, a local temperature jump of 5 K at the center would dissipate in ~200 ns (Figure S14C); for gold and silver, the same temperature jump would dissipate in 2 ns (Figure S14D). Therefore, a SP excitation induced local heating at the gap would dissipate quickly within a single nanostructure, at a time scale 7 to 9 orders of magnitude faster than the average catalytic product generation rate on our nanostructure (every 10 to 30 s per nanostructure). Therefore, at the timescale of catalytic turnovers, a single nanostructure is always thermally homogeneous, with no thermal hotspots that would give rise to the observed catalytic hotspots.

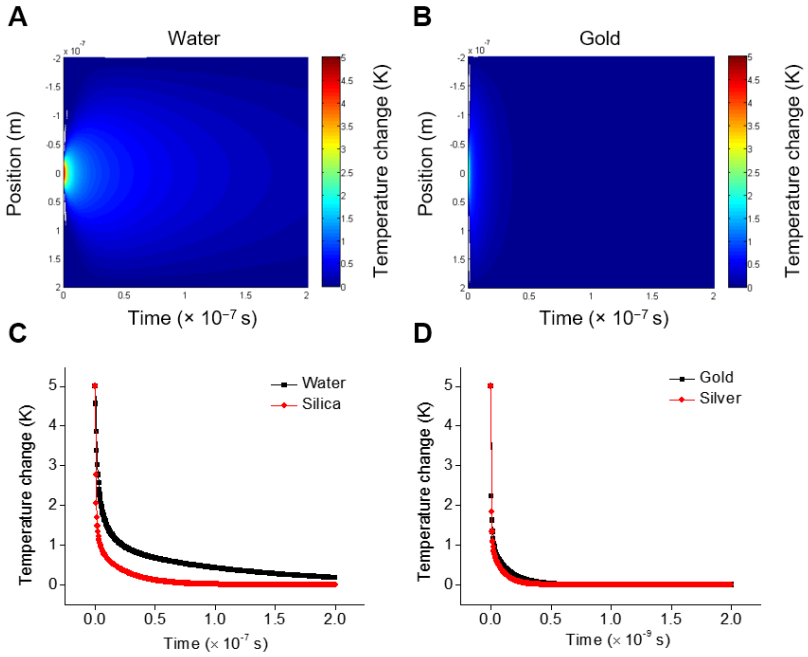

Figure S14. (**A**) Simulation of time-dependent one dimensional temperature profile of water after a local 5 K temperature jump at position 0. (**B**) Same as A, but for gold. (**C**) The temperature change at position 0 with time, showing the heat dissipation rate on water and silica. (**D**) Same as C, but for gold and silver.

S6. FDTD simulations, and additional simulation results

S6.1. General method of FDTD simulation

FDTD simulations were carried out using the simulation package FDTD Solutions from Lumerical Solutions, Inc. Our FDTD simulations use the experimental configuration of our single molecule fluorescence imaging and the nanostructure geometry determined from SEM to obtain the electric field enhancement pattern around every plasmonic nanostructure. The simulations were done in 2-D, to save computational time, as commonly done in the literature[21, 22]. The detailed methods and parameters are described below:

(1) The light sources (i.e., 532 nm and/or 405 nm laser) were always circularly polarized. To generate the circular polarization for each wavelength, two overlapping light sources with orthogonal polarization direction and 90° initial phase difference was applied.[23] Light propagation directions were from the experimental geometry and are in the plane of the nanostructure from the evanescent field excitation from total internal reflection excitation geometry. When two wavelengths were used, their relative powers were taken from experimental values.

(2) The geometry of each gold nanorod in linked nanostructures was taken as a cylinder capped with hemispheres at two ends, of 22 nm in diameter. The length was determined from SEM image. The geometry of silver nanoparticles was taken as a sphere of 50 nm in diameter. Other geometry parameters (e.g. angles between nanorods, relative positions of Ag nanoparticles) were taken directly from SEM image (e.g., Figure S15A-D).

(3) Considering that the spatial resolution of our single-molecule super-resolution imaging was about 40 nm[8], we set the grid size as 1 nm × 1 nm in two-dimensional FDTD simulation, which was 40 times smaller than the spatial resolution. The surrounding environment was set as pure water to simulate the aqueous solution (using silica as environment produced similar results). All dielectric constants were from Palik's Handbook of Optical Constants of Solids.[24]

(4) Electric field enhancement patterns were visualized on the *x*-*y* planes as $|E|^2/|E_0|^2$. To calculate the local electric field enhancement value at the gap and non-gap regions, the electric field enhancement within 3 nm away from the metal surface was used, as the catalytic reactions happen on the surface of metal nanoparticles and the molecules are only ~1 nm in size, and averaged within a circular region centered at the gap or a non-gap region (Figure S15E-F).

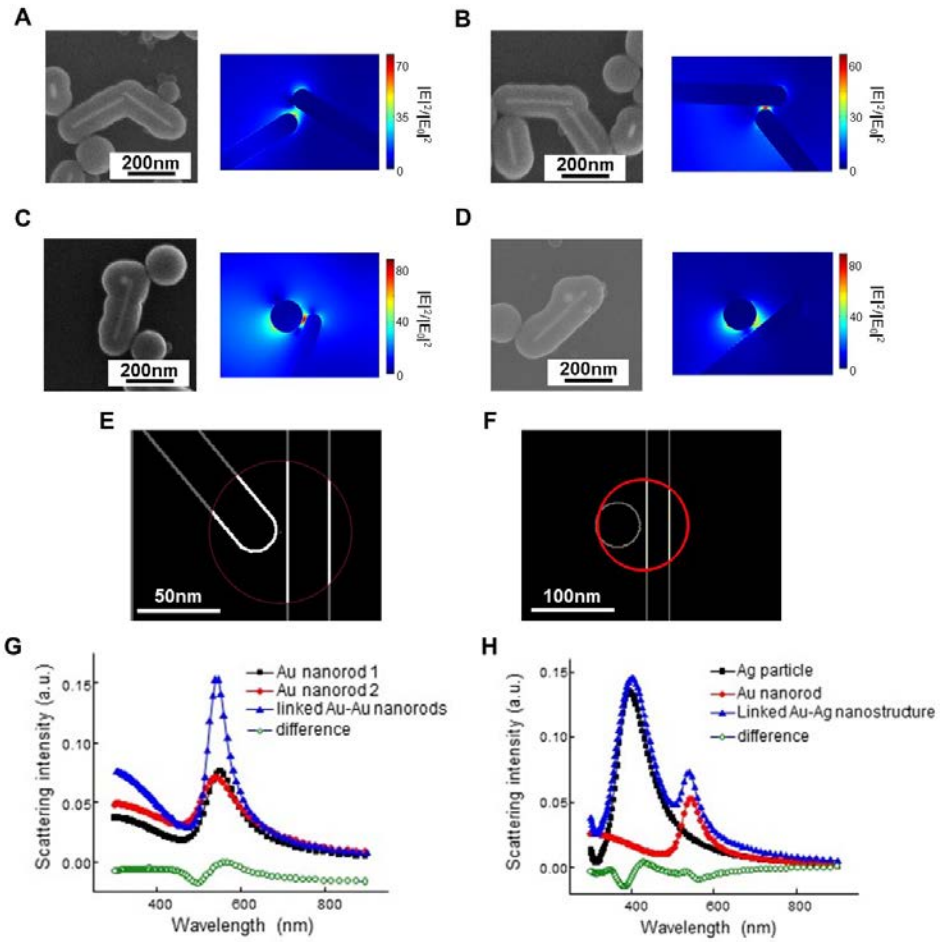

Figure S15. (**A-D**) Additional examples of SEM images of linked Au-Au nanorod (A, B) and Au-Ag nanorod-nanoparticle (C, D) nanostructures and corresponding electric field intensity distribution at 532 nm from FDTD simulation. All scale bars in FDTD simulations are 50 nm. (**E-F**) Averaging electric field enhancement was calculated by averaging the data points located within 3 nm from the Au surface (thick white lines) within a circular region (red line). (**G**) FDTD simulation of the scattering spectra of the linked Au-Au nanorod structure in Figure 2 in the main text (blue) and of the two constituent nanorods individually (black and red), and the difference spectrum (green) between the spectrum of the linked structure and the sum of the two constituents. (**H**) Same as L, but for the linked Au-Ag nanostructure in Figure 4 in the main text.

Scattering spectra simulation. We also used the same software to simulate the scattering spectra of linked nanostructures in comparison with the sum of their individual constituents. Examples are shown in Figure S15G-H. In these simulations, we applied a total-field scattered-field (TFSF) light source with a wavelength range between 300 nm to 900 nm. The propagation direction and polarization of the light source are taken from experimental conditions. The FDTD simulation space is 500 nm × 500 nm in x and y, with mesh size of 1 nm. A cross section analysis monitor group was added in the software to monitor the scattering spectra (as well as absorption and extinction spectra) between 300 nm to 900 nm. (Similar calculation and detailed software setup steps can be found from Lumerical website here.) Because of the TFSF source, the simulation software can compute the power scattered by the nanostructure by measuring the power flow through a box of monitors located in the scattered field region.

The simulation results indicate that the linked Au-Au nanorod has similar scattering spectrum to the sum of the two constituent Au nanorods (Figure S15G), with a peak at ~550 nm. The longitudinal plasmon mode is at >900 nm and beyond our detectable wavelength range. Similarly, the linked Au-Ag nanorod-nanoparticle structure has a similar spectrum to the sum of the constituent Au nanorod and Ag nanoparticle, with two peaks at ~420 nm and ~550 nm, respectively (Figure S15H).

S6.2. Electric field enhancement ratio of gap vs. non-gap regions depends less significantly on the direction of incident light propagation than on the linkage geometry

In the main text, we have shown that the local electric field enhancement ratio at gap vs. non-gap regions depends not only on the gap size, but also on the relative orientation of the two nanorods (i.e., linkage geometry). We also used FDTD simulations to demonstrate that the electric field enhancement ratio of gap vs. non-gap regions does not depend significantly on the propagation direction of incident light. Here, we used the two model geometries of Au-Au and Au-Ag linked nanostructures (Figure S16A-B) in simulation. By changing the angle (φ) between the light propagation direction and the *x*-axis from 0° to 180°, we calculated the electric field enhancement ratio at gap vs. non-gap regions for both nanostructures. The results show that the electric field enhancement ratio varies depending on the angle φ, but the variations between the maximum and minimum enhancements are between 13%-17% for both Au-Au and Au-Ag linked nanostructures, much smaller than the variation (~55-65%) caused by the differences in the gap size (Figure 5B and F) and that (~47%) caused by differences in the relative orientations of the two nanorods (Figure 5D). Therefore, the effect of light propagation direction on local electric field enhancement ratio of gap vs. non-gap is a less significant factor.

In addition, instead of using circularly polarized light, we also performed FDTD simulations using *s* and *p* polarized light, using the linked Au-Au nanorods as a representative example. The results only show small difference from those of circularly polarized light (Figure S16C), and the variation of the enhancement factor across different light propagation directions is still ~17%, much smaller than the variation (~55-65%) caused by the differences in gap sizes.

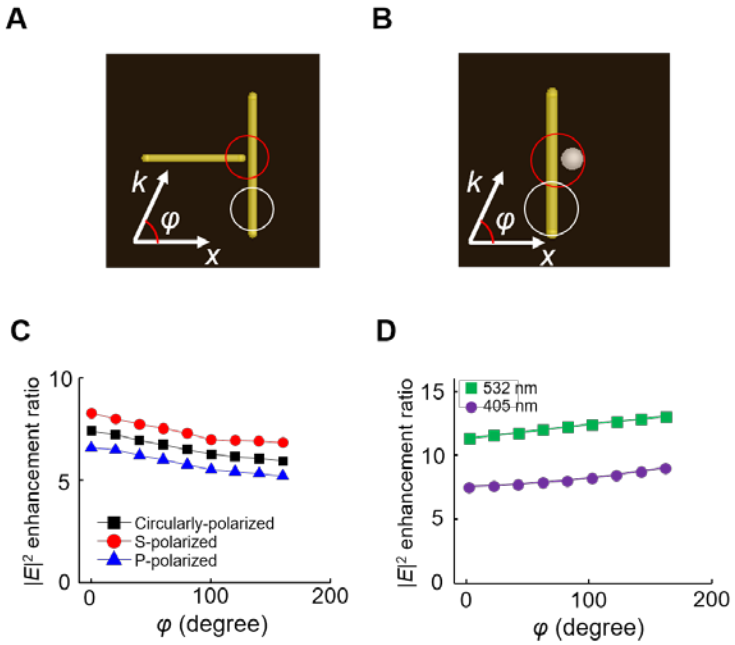

Figure S16. (**A**) Model geometry in FDTD simulations with 532 nm excitation for light propagation direction effect with a 5 nm gap for linked Au-Au nanorods. (**B**) Model geometry in FDTD simulations with simultaneous 532 nm and 405 nm excitation (equal intensities) for light propagation direction effect with a 5 nm gap for linked Au-Ag nanostructures. (**C**) Electric field enhancement ratio at gap vs. non-gap regions as a function of light propagation direction from FDTD simulations of the model Au-Au nanostructure in A, with three different polarization types. (**D**) Same as C but for the model Au-Ag nanostructure in B with two different detection wavelengths.

S6.3. Localization error due to plasmonic antenna effect is less than ~20 nm, significantly smaller than the experimental localization precision of ~40 nm

In our single-molecule imaging experiments, all product molecules are detected around plasmonic nanocatalysts, in which the fluorescence emission could potentially couple to the plasmon resonance of the nanostructure via near-field antenna effect, leading to a shift of the apparent position of the fluorescent molecule from its actual position. This antenna-effect typically cause an apparent position shift of ~20 nm of individual molecules,[21] smaller than our experimental localization precision (~40 nm) and much smaller than the circle diameter (80, 140, or 200 nm) that we use in picking out gap and non-gap regions. Therefore, we expect this antenna effect has no significant influence in our mapping the product locations on individual linked Au-Au and Au-Ag nanostructures. Nevertheless, in order to evaluate the potential localization error due to the plasmonic antenna effect, we carried out FDTD simulations on fluorescence emission from this molecule-antenna hybrid to quantify the effect.

In these FDTD simulations, a dimensionless emissive dipole was used to model a resorufin product molecule, emitting at 580 nm, the center wavelength of the optical bandpass filter in detecting the fluorescence of resorufin in our single-molecule imaging experiments. We used a T-shaped Au-Au nanorod linkage structure with 5 nm gap size as an example (Figure S17C). The dipole orientation was set to be one of the three orthogonal directions in a 3-dimensional space (parallel to *x*, *y* or *z* axis), while the distance between the dipole and the gold nanorod surface was set to be 5 nm to emulate the scenario of molecule-antenna hybrids (Positions 1, 2, and 3 in Figure S17C). As a comparison, another position of the emitting dipole at 100 nm away from Position 1 and 3 was also simulated (Position 4 in Figure S17C). For each geometry, the near-field electromagnetic intensity was calculated (e.g., Figure S17A). The far-field image was obtained by calculating the Fourier transform of Poynting vector within a certain monitoring volume and then applying an objective with a numerical aperture of 1.2 to mimic the image acquisition process in experiments. Then, the far-field image was fitted by a 2D Gaussian function to determine the apparent centroid location of the molecule (Figure S17B), which can be compared with the actual position of the molecule in the simulation input. In Figure S17D, the results show that the apparent centroid position of the molecule is shifted by less than 20 nm from its actual position in all simulated cases, which is significantly less than the average localization precision of our single-molecule experiments (~40 nm). This verifies that the antenna effect around plasmonic nanostructures in our experiments would not change significantly the mapping of the catalytic product molecules.

As a comparison and control to our FDTD simulations here, we also repeated the simulations by Uji-i and coworkers[21] , in which an emitting molecular dipole was positioned at three different positions and 5 nm away from the surface of a Au nanorod of 70 nm in length and 30 nm in diameter (Figure S17E-G). (Note this nanorod is much smaller than the Au nanorods we studied here (~20 nm in diameter and hundreds of nanometer in length). The calculated corresponding far-field emission images from the near-field electric field intensity patterns are shown in Figure S17H-J. The center positions of these far-field images are about 17 to 33 nm shifted from the actual molecular positions because of the plasmonic antenna effect. This magnitude of ~17 to 33 nm localization error is consistent with our FDTD simulations on linked Au-Au nanorods (Figure S17D), but for the particular system of Uji-i, it becomes problematic because it is now comparable to the dimension of the Au nanorod (70 × 30 nm), making mapping the molecular position relative to the nanorod unreliable.

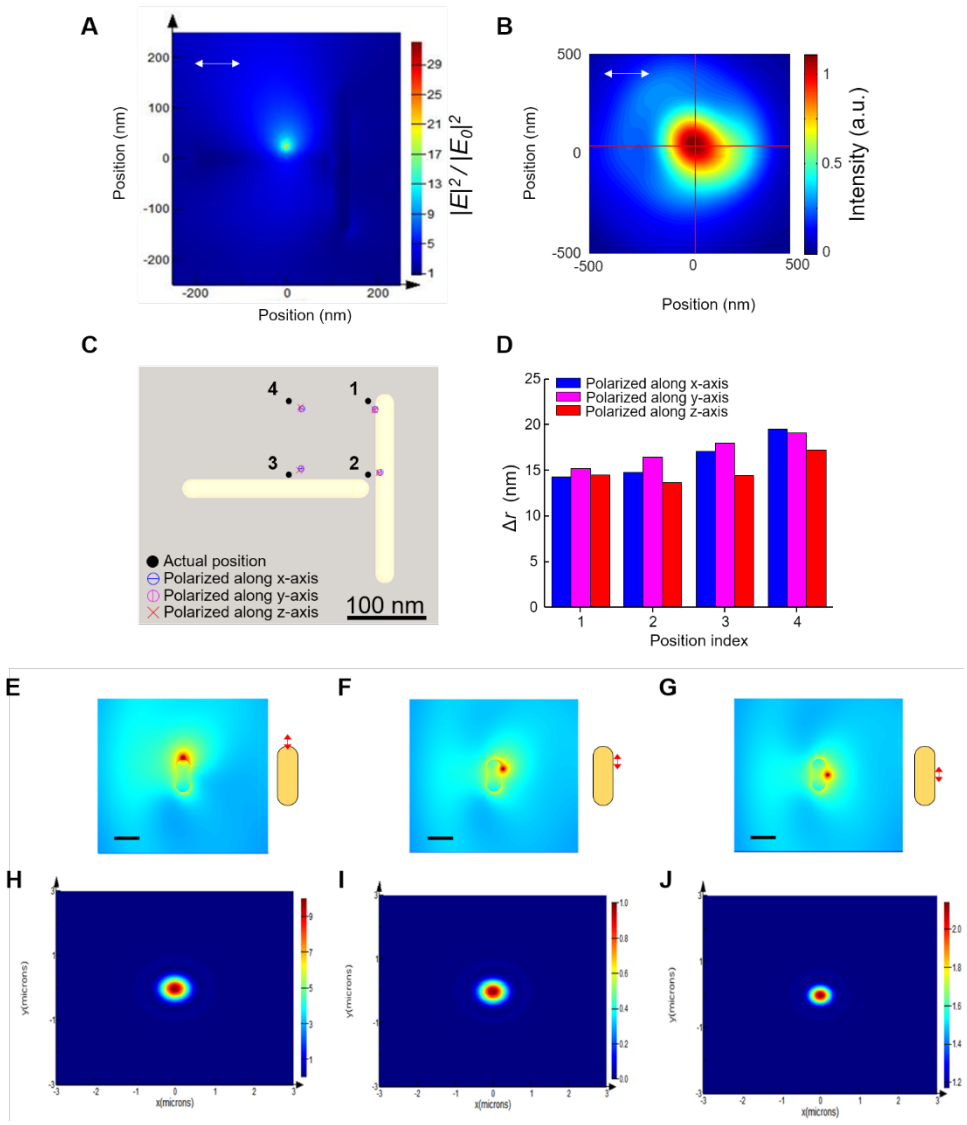

Figure S17. FDTD simulations on localization error due to plasmon antenna effect. (**A**) Near-field electric field intensity pattern around a T-shaped Au-Au nanorod linkage structure with an emitting dipole polarized along *x*-axis at Position 3 in C. (**B**) Corresponding far-field emission image of A and a 2D Gaussian fit to determine the centroid position (cross of the two red lines). (C) Comparison between actual molecule positions and apparent positions from the far-field imaging for all simulated cases with different emitting dipole positions and polarization directions. (**D**) Location differences between actual positions and apparent positions. (**E-G**) Near-field electric field intensity distributions of an emitting dipole at three different positions around a Au nanorod of 70 nm in length and 30 nm in diameter. Scale bar = 50 nm. The schemes on the right show the three positions of the emitting dipole at 5 nm away from the Au surface and polarized parallel to the nanorod long axis. (**H-J**) The calculated far-field emission images corresponding to E-G. The differences between the actual emitting dipole positions and the centroid locations of their far-field images are 33.4 nm, 26.5 nm, and 17.2 nm, respectively.

S7. Nanocatalyst surface area calculation within observation circles

S7.1. Approximation of Au surface areas of linked Au-Au and Au-Ag nanostructures

For the calculation of Au nanorod surface area inside an observation circle, we first estimated the surface area through its geometry. Figure S18 shows typical linkage geometries of linked Au-Au nanorod structures, in which *C* is the center position of the gap; *O* is the center position of the hemisphere cap of Au nanorod; *K's* are the crossing points of the observation circle and the nanorod's central axes; *CM's* represent the vertical distances between the gap center and the central axes of the nanorods.

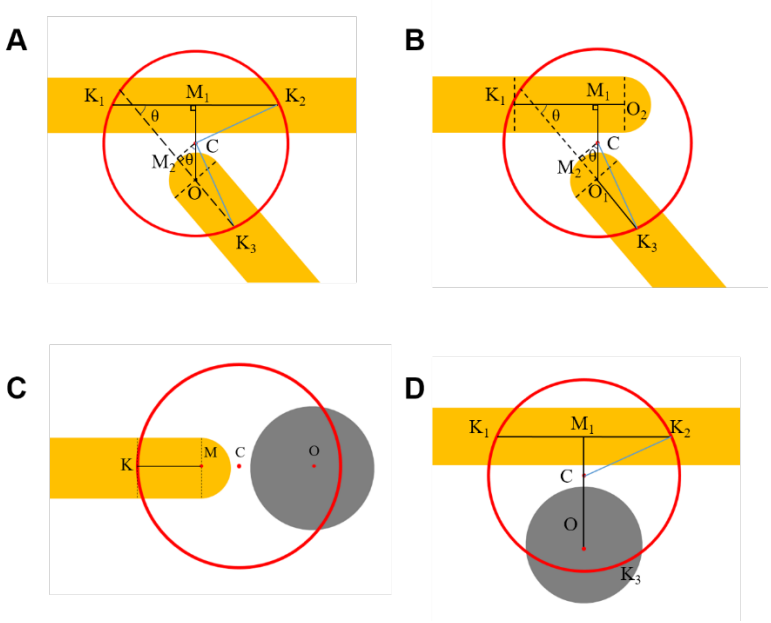

Figure S18. Typical linkage geometries of (**A, B**) Au-Au nanorod-nanorod and (**C, D**) Au-Ag nanorod-nanoparticle structures.

For the geometry in Figure S18A, total surface area within the red circle is from adding two nanorods' surface area. The surface area of one nanorod in the circle is approximated by the side surface area of a cylinder with a length of K_1K_2. The surface area of the other nanorod is approximated by adding a hemisphere surface area and a cylinder with a length of OK_3.

Setting the diameter of nanorods as d, the gap size as G, the angle between two nanorods as θ, and the radius of observation circle as R, the surface area of the hemisphere is $\frac{\pi d^2}{2}$. The surface area of the two cylinders are $\pi d(K_1K_2+OK_3)$. The total nanorod surface area in the observation circle in Figure S18A is then:

$$S_A = \frac{\pi d^2}{2} + \pi d(K_1K_2+OK_3)$$

And

$$K_1K_2 = 2M_1K_2 = 2\sqrt{CK_2{}^2 - CM_1{}^2} = 2\sqrt{R^2 - \left(\frac{d+G}{2}\right)^2}$$

Since

$$CO = \frac{d+G}{2}$$

$$CM_2 = CO \cdot \cos\theta = \frac{d+G}{2} \cdot \cos\theta$$

$$OM_2 = CO \cdot sin\theta = \frac{d+G}{2} \cdot sin\theta$$

$$M_2K_3 = \sqrt{{CK_3}^2 - {CM_2}^2} = \sqrt{R^2 - \left(\frac{d+G}{2} \cdot \cos\theta\right)^2}$$

$$OK_3 = M_2K_3 - OM_2 = \sqrt{R^2 - \left(\frac{d+G}{2} \cdot \cos\theta\right)^2} - \frac{d+G}{2} \cdot sin\theta$$

Therefore,

$$S_A = \frac{\pi d^2}{2} + \pi d\left(2\sqrt{R^2 - \left(\frac{d+G}{2}\right)^2} + \sqrt{R^2 - \left(\frac{d+G}{2} \cdot \cos\theta\right)^2} - \frac{d+G}{2} \cdot sin\theta\right) \quad \text{(S11)}$$

For the geometry in Figure S18B, the surface area was obtained by adding two nanorods' surface area as well. Each nanorod is approximated by adding a hemisphere surface area and a cylinder of length of O_2K_1 or O_1K_3. By applying the same variables as the above calculation, the total nanorod surface area in observation circle in Figure S18B is:

$$S_B = \pi d^2 + \pi d(O_2K_1 + O_1K_3)$$

And

$$O_1K_3 = M_2K_3 - O_1M_2 = \sqrt{R^2 - \left(\frac{d+G}{2} \cdot \cos\theta\right)^2} - \frac{d+G}{2} \cdot sin\theta$$

Therefore

$$S_B = \pi d^2 + \pi d\left(O_2K_1 + \sqrt{R^2 - \left(\frac{d+G}{2} \cdot \cos\theta\right)^2} - \frac{d+G}{2} \cdot sin\theta\right) \quad \text{(S12)}$$

For the linked Au-Ag geometries in Figure S18C and Figure S18D, because only Au is catalytically active, we calculated the surface area of only the Au nanorod within the observation circle. Similarly, as we did above, for that in Figure S18C, we get:

$$S_C = \frac{\pi d^2}{2} + \pi d \cdot KM = \frac{\pi d^2}{2} + \pi d \cdot (CK - CM) = \frac{\pi d^2}{2} + \pi d \cdot \left(R - \frac{d+G}{2}\right) \quad \text{(S13)}$$

And

$$S_D = \pi d \cdot K_1K_2 = \pi d \cdot 2M_1K_2 = \pi d \cdot 2\sqrt{R^2 - \left(\frac{d+G}{2}\right)^2} \quad \text{(S14)}$$

S7.2. Validation of approximation via numerical surface integration

To verify the above surface area approximations for the cylinder portion of the nanorods, we applied a surface integral of intersection of two cylinders to obtain the exact surface areas of the nanorods within the observation circle (Figure S19A). Specifically, the bigger cylinder in Figure S19A is the observation circle whose diameter can be 80 nm, 140 nm or 200 nm. The smaller one is a Au nanorod. The purpose here is to calculate the surface area of the smaller cylinder within the intersection with the bigger cylinder.

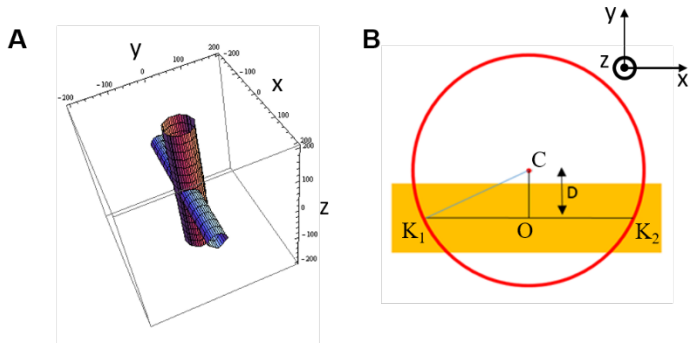

Figure S19. Surface integral of intersection to calculate the exact surface area of nanorod in an observation circle. (**A**) The intersection model of surface area calculation. One smaller cylinder along the *x*-axis represents the nanorod; the other bigger cylinder along the *z*-axis represents the observation circle, with the distance between the two axes being *D*. (**B**) Cross section of the model in A in the *xy* plane. Red circle represents the observation circle. Yellow rectangle represents the gold nanorod.

Figure S19A presents a common scenario where the smaller cylinder (radius *r*) goes through the bigger cylinder (radius *R*) in a perpendicular manner, oriented long the *x*- and *z*-axis, respectively. The distance between the central axes of Au nanorod and observation circle is *D*. In three-dimensional space, we set the center position of Au nanorod as the origin (position O in Figure S19B). Then, the surface of the two cylinders follow these equations, respectively:

$$\begin{cases} y^2 + z^2 = r^2 \\ x^2 + (y - D)^2 = R^2 \end{cases} \tag{S15}$$

Then, we have:

$$\begin{cases} x = \pm\sqrt{R^2 - (\sqrt{r^2 - z^2} - D)^2} \\ y = \pm\sqrt{r^2 - z^2} \end{cases} \tag{S16}$$

In order to calculate the surface area of the Au nanorod (smaller cylinder) inside the intersection of the two cylinders, we used the method described by Weisstein[25]. The intersected surface area can be calculated by the surface integral as:

$$S_{int} = 8\int_0^r \left|\frac{x}{y}\right| r dz = 8\int_0^r \sqrt{R^2 - (\sqrt{r^2 - z^2} - D)^2}\,\frac{r}{\sqrt{r^2 - z^2}}\,dz \quad \text{(S17)}$$

Specially, if $D = 0$, we can calculate the analytical solution of Equation (S17):

$$S_{int} = 8r\sqrt{R^2 - r^2}\,\text{EllipticE}\left[\frac{r^2}{r^2 - R^2}\right] \quad \text{(S18)}$$

in which "EllipticE" is the complete elliptic integral which can be solved numerically. Otherwise, if $D \neq 0$, we can calculate the numerical integration of S_{int} after knowing the *r*, *R*, *D* values.

Meanwhile, we can also estimate the surface area of Au nanorod inside in the observation circle in Figure S19B using the same approximate method as in Section S7.1. In this model, intersected surface area of nanorod is approximated by the surface area of a cylinder with the same diameter of nanorod and with length of K_1K_2, similarly as in Equation (S14). Hence the approximation surface area is:

$$S_{ap} = 4\pi r\sqrt{R^2 - D^2} \quad \text{(S19)}$$

By using the two methods above and applying the size of nanorod, observation circle, and D = 15 nm (i.e., assuming a gap size of 5 nm, close to the smallest gap size we experimentally observed), we have:

Table S2. Surface area difference from integral calculation and approximation with a gap size of 5 nm.

R (nm)	40	70	100
Integral calculation (nm^2)	6154.1	10905.7	15657.2
Approximation (nm^2)	5824.5	10739.8	15529.8
Error (%)*	5.36	1.52	0.81

* Error (%)= | (Integral calculation) – (Approximation) | / (Integral calculation) ×100%

By using the two methods above and applying the size of nanorod, observation circle and D = 20 nm (i.e., assuming a gap size of 15 nm, close to the largest gap size we experimentally observed), we have:

Table S3. Surface area difference from integral calculation and approximation with a gap size of 15 nm.

R (nm)	40	70	100
Integral calculation (nm^2)	5957.4	10814.2	15581.7
Approximation (nm^2)	5441.4	10537.2	15390.6
Error (%)	8.66	2.56	1.22

Hence, the value difference of surface area from integral calculation and approximation is always less than 10%. When we chose 70 nm as the radius of observation circle to evaluate specific activity of Au nanorods, the error was even less than 3%. Therefore, it is reasonable to approximately calculate surface

area of catalysts by using Equations (S11) or (S12) for linked Au-Au nanorods structures and Equations (S13) or (S14) for linked Au-Ag nanorod-nanoparticle structures, which were used for calculating the specific activities reported in the main text.

S8. Specific turnover rate follows a second order dependence on the excitation light power density (Figure S20 and Table S4)

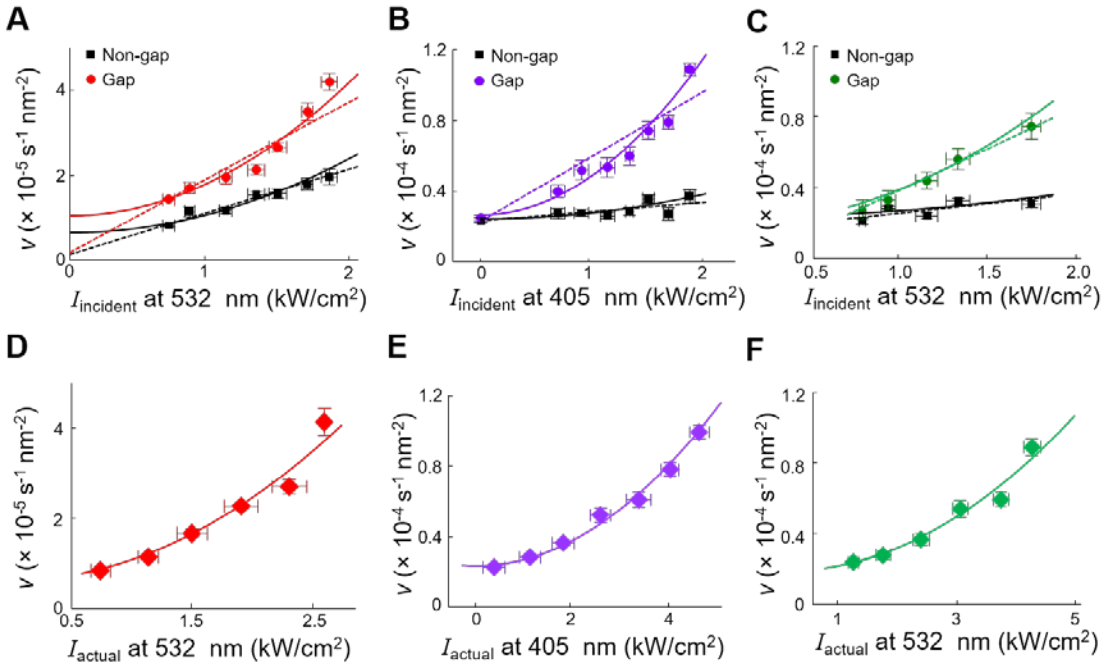

Figure S20. Comparison between the linear and quadratic fittings on the specific activity vs. local incident power density or local actual power density. The data presented here are the same as Fig. 6 in the main text, but only the binned and averaged data points are reporudced here. Fitting parameters are summarized in Table S4. (**A**) Specific turnover rates *v* of linked Au-Au nanorods at gap and non-gap regions vs. their local incident light power density $I_{incident}$ at 532 nm. Solid lines: quadratic fits; dashed lines: linear fits (**B**) Same as A, but for linked Au-Ag nanorod-nanoparticle structures and for 405 nm light. (**C**) Same as B, but for 532 nm light. (**D-F**) Corresponding to A-C respectively, in which the incident local light power density has been converted to the actual local power density using the electric field enhancement factor obtained from FDTD simulations. *x* error bars are s.d.; *y* error bars are s.e.m.

Table S4. Comparisons of fitting parameters from Figure S20. All linear fittings use the equation $v = A_L + B \cdot I$, while all quadratic fittings use the equation $v = A_Q + C \cdot I^2$, in which v is the specific turnover rate and I is the power density. In all cases, the quadratic fitting has a higher R^2 value (green numbers) than the corresponding linear fitting, indicating that the second order relationship between activity and light power density fits the data better. Note both fittings are two-parameter fits; so, the degrees of freedoms are the same. Moreover, for the linear fits, A_L, which corresponds to the extrapolated specific activity at zero light illumination sometimes becomes negative for the gap region, further supporting the unreasonableness/inadequacy of the linear fits. Furthermore, the specific turnover rates of the gap regions fall on the same curve as those for the non-gap regions as a function of increasing actual local power density in all cases (red numbers). These results further demonstrate that the underlying mechanism of the plasmonic catalytic enhancement involves two photoexcited species.

		Gap (local power density)	Non-gap (local power density)	Actual power density
Au-Au 532nm	$A_Q(\times10^{-5}\ s^{-1}\ nm^{-2})$	1.04±0.06	0.64±0.06	0.61±0.06
	C ($\times10^{-1}\ m^2\ W^{-2}\ s^{-1}$)	0.89±0.08	0.49±0.05	0.50±0.03
	R_Q^2	0.961	0.942	0.976
	$A_L(\times10^{-5}\ s^{-1}\ nm^{-2})$	-0.39±0.45	0.23±0.11	N/A
	B ($\times10^{6}\ W^{-1}\ s^{-1}$)	2.39±0.35	0.99±0.08	
	R_L^2	0.921	0.862	
Au-Ag 405nm	$A_Q(\times10^{-5}\ s^{-1}\ nm^{-2})$	2.56±0.22	2.39±0.15	2.29±0.09
	C ($\times10^{-1}\ m^2\ W^{-2}\ s^{-1}$)	2.55±0.16	0.38±0.11	0.42±0.02
	R_Q^2	0.973	0.617	0.936
	$A_L(\times10^{-5}\ s^{-1}\ nm^{-2})$	0.16±0.08	0.23±0.28	N/A
	B ($\times10^{6}\ W^{-1}\ s^{-1}$)	0.43±0.67	0.61±0.22	
	R_L^2	0.853	0.452	
Au-Ag 532nm	$A_Q(\times10^{-5}\ s^{-1}\ nm^{-2})$	1.64±0.28	2.27±0.37	1.95±0.22
	C ($\times10^{-1}\ m^2\ W^{-2}\ s^{-1}$)	2.23±0.20	0.34±0.02	0.39±0.03
	R_Q^2	0.968	0.491	0.962
	$A_L(\times10^{-5}\ s^{-1}\ nm^{-2})$	-1.29±0.25	1.68±0.61	N/A
	B ($\times10^{6}\ W^{-1}\ s^{-1}$)	5.30±0.22	0.92±0.52	
	R_L^2	0.954	0.349	

Additional references

1. Jana, N. R.; Gearheart, L.; Murphy, C. J., Wet Chemical Synthesis of High Aspect Ratio Cylindrical Gold Nanorods. *J. Phys. Chem. B* **2001,** *105*, 4065-4067.
2. Wang, Z. L.; Mohamed, M. B.; Link, S.; El-Sayed, M. A., Crystallographic Facets and Shapes of Gold Nanorods of Different Aspect Ratios. *Surf. Sci.* **1999,** *440*, L809-L814.
3. Zhou, X.; Andoy, N. M.; Liu, G.; Choudhary, E.; Han, K.-S.; Shen, H.; Chen, P., Quantitative Super-Resolution Imaging Uncovers Reactivity Patterns on Single Nanocatalysts. *Nat. Nanotechnol.* **2012,** *7*, 237-241.
4. Caswell, K. K.; Wilson, J. N.; Bunz, U. H. F.; Murphy, C. J., Preferential End-to-End Assembly of Gold Nanorods by Biotin−Streptavidin Connectors. *J. Am. Chem. Soc.* **2003,** *125*, 13914-13915.
5. Stöber, W.; Fink, A.; Bohn, E., Controlled Growth of Monodisperse Silica Spheres in the Micron Size Range. *J. Colloid Interface Sci.* **1968,** *26*, 62-69.
6. Andoy, N. M.; Zhou, X.; Choudhary, E.; Shen, H.; Liu, G.; Chen, P., Single-Molecule Catalysis Mapping Quantifies Site-Specific Activity and Uncovers Radial Activity Gradient on Single 2d Nanocrystals. *J. Am. Chem. Soc.* **2013,** *135*, 1845-1852.
7. Aliaga, C.; Park, J. Y.; Yamada, Y.; Lee, H. S.; Tsung, C.-K.; Yang, P.; Somorjai, G. A., Sum Frequency Generation and Catalytic Reaction Studies of the Removal of Organic Capping Agents from Pt Nanoparticles by Uv−Ozone Treatment. *J. Phys. Chem. C* **2009,** *113*, 6150-6155.

8. Zhou, X.; Choudhary, E.; Andoy, N. M.; Zou, N.; Chen, P., Scalable Parallel Screening of Catalyst Activity at the Single-Particle Level and Subdiffraction Resolution. *ACS Catal.* **2013,** *3*, 1448-1453.
9. Djokić, S.; Nikolić, N.; Živković, P.; Popov, K.; Djokić, N., Electrodeposition and Electroless Deposition of Metallic Powders: A Comparison. *ECS Trans.* **2011,** *33*, 7-31.
10. Kuzuya, A.; Numajiri, K.; Kimura, M.; Komiyama, M., Single-Molecule Accommodation of Streptavidin in Nanometer-Scale Wells Formed in DNA Nanostructures. *Nucleic Acids Symp Ser (Oxf)* **2008**, 681-682.
11. Xiaoge, H.; Wenlong, C.; Tie, W.; Erkang, W.; Shaojun, D., Well-Ordered End-to-End Linkage of Gold Nanorods. *Nanotechnology* **2005,** *16*, 2164.
12. Paramelle, D.; Sadovoy, A.; Gorelik, S.; Free, P.; Hobley, J.; Fernig, D. G., A Rapid Method to Estimate the Concentration of Citrate Capped Silver Nanoparticles from Uv-Visible Light Spectra. *Analyst* **2014,** *139*, 4855-4861.
13. Awazu, K.; Fujimaki, M.; Rockstuhl, C.; Tominaga, J.; Murakami, H.; Ohki, Y.; Yoshida, N.; Watanabe, T., A Plasmonic Photocatalyst Consisting of Silver Nanoparticles Embedded in Titanium Dioxide. *J. Am. Chem. Soc.* **2008,** *130*, 1676-1680.
14. Xu, W.; Kong, J. S.; Yeh, Y.-T. E.; Chen, P., Single-Molecule Nanocatalysis Reveals Heterogeneous Reaction Pathways and Catalytic Dynamics. *Nat. Mater.* **2008,** *7*, 992-996.
15. Thompson, R. E.; Larson, D. R.; Webb, W. W., Precise Nanometer Localization Analysis for Individual Fluorescent Probes. *Biophys. J.* **2002,** *82*, 2775-2783.
16. Yildiz, A.; Forkey, J. N.; McKinney, S. A.; Ha, T.; Goldman, Y. E.; Selvin, P. R., Myosin V Walks Hand-over-Hand: Single Fluorophore Imaging with 1.5-Nm Localization. *Science* **2003,** *300*, 2061-2065.
17. D Axelrod; T P Burghardt, a.; Thompson, N. L., Total Internal Reflection Fluorescence. *Annu. Rev. Biophys. Bioeng.* **1984,** *13*, 247-268.
18. Saleh, B. E. A.; Teich, M. C., *Fundamentals of Photonics*. Wiley: 2007.
19. Firoozabadi, A.; Ghorayeb, K.; Shukla, K., Theoretical Model of Thermal Diffusion Factors in Multicomponent Mixtures. *AIChE J.* **2000,** *46*, 892-900.
20. Govorov, A. O.; Richardson, H. H., Generating Heat with Metal Nanoparticles. *Nano Today* **2007,** *2*, 30-38.
21. Su, L.; Yuan, H.; Lu, G.; Rocha, S.; Orrit, M.; Hofkens, J.; Uji-i, H., Super-Resolution Localization and Defocused Fluorescence Microscopy on Resonantly Coupled Single-Molecule, Single-Nanorod Hybrids. *ACS Nano* **2016,** *10*, 2455-2466.
22. Zheng, Z.; Tachikawa, T.; Majima, T., Plasmon-Enhanced Formic Acid Dehydrogenation Using Anisotropic Pd–Au Nanorods Studied at the Single-Particle Level. *J. Am. Chem. Soc.* **2015,** *137*, 948-957.
23. https://kb.lumerical.com/en/ref_sim_obj_planewave_circular_polarization.html.
24. List of Contributors for Volume I A2 - Palik, Edward D. In *Handbook of Optical Constants of Solids*, Academic Press: Burlington, 1997; pp xv-xvi.
25. Weisstein, E. W. "Steinmetz Solid." From Mathworld--a Wolfram Web Resource. http://mathworld.wolfram.com/SteinmetzSolid.html.